Effects of Grain Size and Orientation on Mechanical Response of Lead Free Solders

by

Jing Zou

A thesis submitted to the Graduate Faculty of
Auburn University
in partial fulfillment of the
requirements for the Degree of
Master of Science

Auburn, Alabama
December 14, 2013

Keywords: lead-free solder, sub-grain size, grain orientation,
mechanical properties, aging, microstructure

Approved by

Jeffrey C. Suhling, Chair, Quina Distinguished Professor of Mechanical Engineering
Barton C. Prorok, Professor of Mechanical Engineering
Michael J. Bozack, Professor of Physics

Abstract

In this study, the effects of grain size and orientation on mechanical behaviors of lead free solders were evaluated by measuring the sub-grain size and determining the plane orientation of the grains. Sn-Ag-Cu (SAC) solder alloys and solder joints (SAC 105, SAC 305, SACX) were chosen for investigation. By using polarized light microscopy, Ball Grid Array (BGA) solder joints were found to typically be comprised of a single grain or just a few grains. To quantitatively measure the sub-grain size, three methods including the intercept method, the planimetric method, and the electron backscatter diffraction (EBSD) method were applied to examine the microstructure of SAC solders. The results indicated that the sub-grain size increased during aging, which could be a cause of aging-induced degradation of mechanical properties of SAC solders.

In the second part of this work, the grain orientations in solder specimens and joints were characterized by the EBSD technique. Inverse pole figures (IPFs) were generated and used to calculate the Euler angles and crystallographic orientations of the grains. Based on the determination of the crystallographic orientations, the elastic modulus values were determined in the global coordinate directions of the joints. Simple finite element models were also developed to show the importance of the grain structure and orientation. The results revealed that in-plane shear stress concentrations were induced along the grain boundaries and the stress distributions were dependent on the grain sizes and orientations in the SAC solder joints.

Acknowledgments

First, I would like to dedicate this thesis to my parents, Jinxiang Zou and Qiuyun Zhang. Without their continued support and encouragement of me, I would not have had this chance to perform this project and earn my M.S. degree. They understood my decisions and gave me endless love even though we are living in different countries.

I am heavily grateful to my major advisor Dr. Jeffrey C. Suhling for his sincere trust on me, teaching me to have a professional attitude towards research. He gave me the ability to overcome the difficulties that I faced in my work. Special thanks are also given to Dr. Barton C. Prorok and Dr. Michael J. Bozack for their invaluable guidance and suggestions for this research.

Finally, I am appreciative of the help from all of our group members, especially Dr. Zijie Cai. He provided me a good example and brought me into performing research in electronic packaging. Thanks to all my friends in Auburn not mentioned here. You took care me a lot and gave me a second home.

Table of Contents

List of Tables

List of Figures

CHAPTER 1

INTRODUCTION

1.1 Lead Free Solders

The performance and quality of solders are important to the functioning of various levels of electronic packaging, like flip-chip connection, solder-ball connection in ball-grid-arrays (BGA), or IC package assembly to a print circuit board (PCB) [1-3]. Sn-Pb alloys have been commonly used in packaging for a long time, playing a crucial role for metal interconnection in the assembly of modern electronic circuits. The eutectic or near-eutectic 63Sn–37Pb solder has many advantages over other alloying elements, like ease of handling, low melting temperature, good workability, ductility, and excellent wetting on copper and its alloys [4].

However, environmental and health issues have hindered the continued widespread use of leaded solders. Legislations such as the Waste in Electrical and Electronic Equipment (WEEE) and the Restriction of the Use of Certain Hazardous Substances (RoHS) have been effective for creating bans on lead in electronic products since August 2005 and July 2006, respectively [5].

Lead free solders with high Sn content are considered as the most promising replacements for lead based solders [6]. To provide leadership in the development of manufacturing for lead-free electronics, the National Electronics Manufacturing Initiative (NEMI) created a project (the so-called NEMI lead-free assembly project) and helped to

open a forum about lead-free electronic assembly at the IPC Works'99 Conference [7]. The IPC Market Research Group has reported worldwide consumption of tin/lead versus lead free solder. Figure 1.1 shows the demand for lead free solders has increased in the global solder industry, from 62 percent in 2008 to 68 percent in 2012.

Some criteria were proposed for leading lead-free alternative solders such as having a melting temperature similar to Sn-Pb solders, being nontoxic, having adequate wetting properties to standard metallizations, having adequate physical and mechanical properties, having good electrical performance, and being relatively inexpensive [9]. Most options for lead-free solders involve tin (Sn) as the base material, and the Sn–Ag–Cu (SAC) series alloys have emerged as a promising alternative that are widely accepted in the electronics industry [10, 11]. Typical SAC alloys include 99Sn-0.3Ag-0.7Cu (SAC0307), 98.5Sn-1.0Ag-0.5Cu (SAC105), 97.5Sn-2.0Ag-0.5Cu (SAC205), 96.5Sn-3.0Ag-0.5Cu (SAC305), 95.5Sn-3.8Ag-0.7Cu (SAC387), 95.5Sn-3.9Ag-0.6Cu (SAC396), and 95.5Sn-4.0Ag-0.5Cu (SAC405).

1.2　Microstructure of SnAgCu (SAC) Solders

Unlike Sn-Pb solders, which can be treated as homogeneous and isotropic materials, SnAgCu (SAC) solders are strongly Sn-based, with a Sn content typically over 95 wt.%. One SAC solder joint typically has just one or only a few anisotropic β-Sn grains, which can be identified using a polarized light microscope.
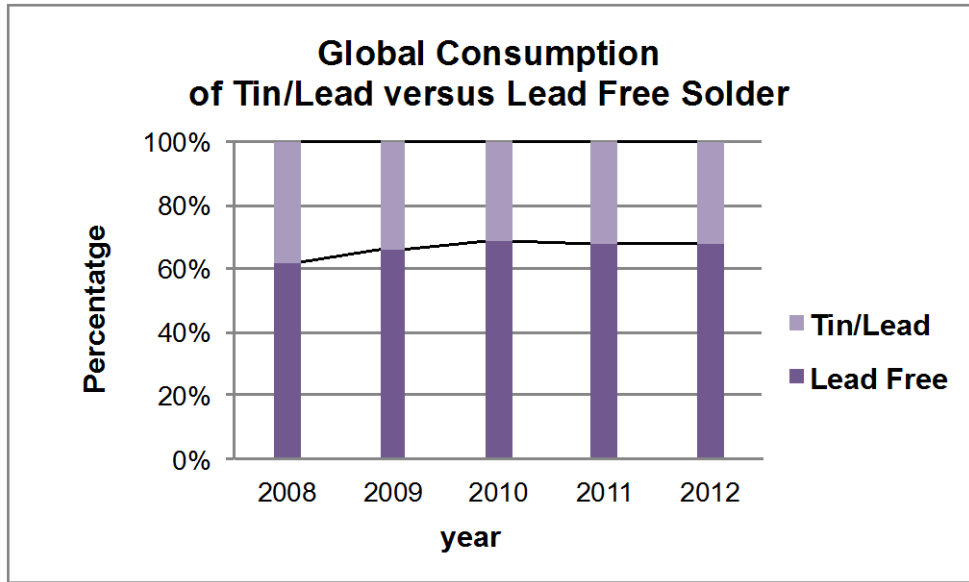
Figure 1.1 Global Consumption of Tin/Lead Versus Lead Free Solder

Figure 1.2 shows a typical multi-grain structure in a SAC305 Ball Grid Array (BGA) solder joint. This photo was taken using an OLYMPUS BX60 optical microscope equipped with an analyzer/polarizer. Grains were identified by different light colors. The pictured structure is a so called "beach ball" pattern, which has been previously reported to be composed of six twin regions turning on the [100] axis in 60° increments [12]. Figure 1.3 shows the left part of the same solder ball. It is observed that the solder ball consists of a β-Sn phase with a fine dispersion of Cu_6Sn_5 and Ag_3Sn intermetallics (IMC) as a second phase. Within a typical β-Sn dendrite, the structure of sub-grains was observed in this work by etching using a chemical solution of 5% hydrochloride and 95% methanol, as illustrated in Figure 1.4. The microstructure of a SAC solder can be treated as a surrounding precipitation of Cu_6Sn_5 and Ag_3Sn (IMC) that hardens a β-Sn matrix (dendrite).

1.3   Elastic Anisotropy of β-Sn

β-Sn has a body-centered tetragonal (BCT) structure, with a = 0.58197 nm, c = 0.31749 nm, and c/a = 0.54553, with atomic positions (0 0 0), (0 0.5 0.25), (0.5 0 0.75) and (0.5 0.5 0.5) [13], as shown in Figure 1.5. The length of a in the [1 0 0] or [0 1 0] direction is almost twice the length of c in the [001] direction. Since Sn is anisotropic and the major constituent of a SAC solder joint, the solder material cannot be treated as homogenous and isotropic, like Sn-Pb solder. This anisotropic nature of the Sn lattice structure leads to the different mechanical and thermal responses for grains with different orientations in the solder joint. Erinc, et al. [14] reported anisotropy of β-Sn induced localized deformations especially along Sn grain boundaries and formed intergranular fatigue cracks, which affects the thermal fatigue life during thermal cycling. Simulation
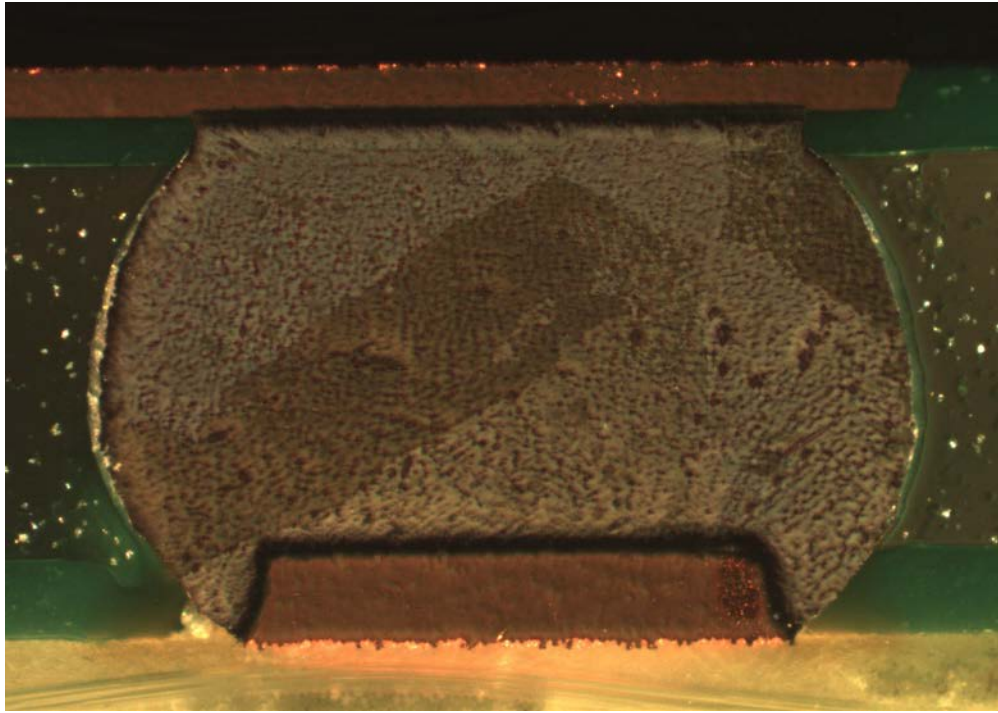
Figure 1.2 Polarized Light Image of a SAC 305 Solder Joint
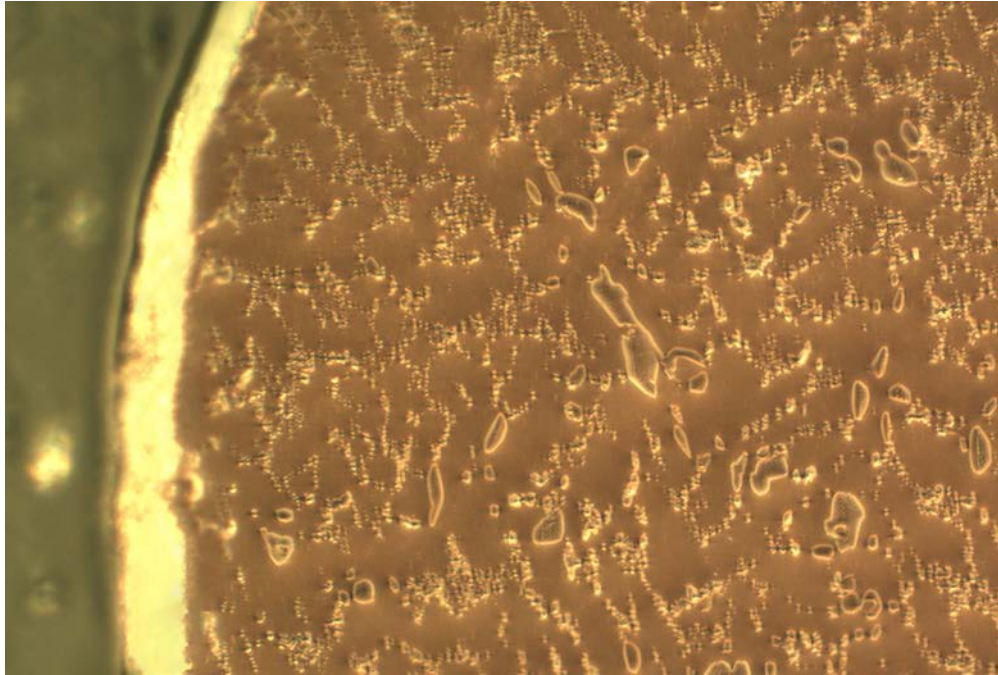
Figure 1.3 Distribution of IMC in a SAC 305 Solder Joint
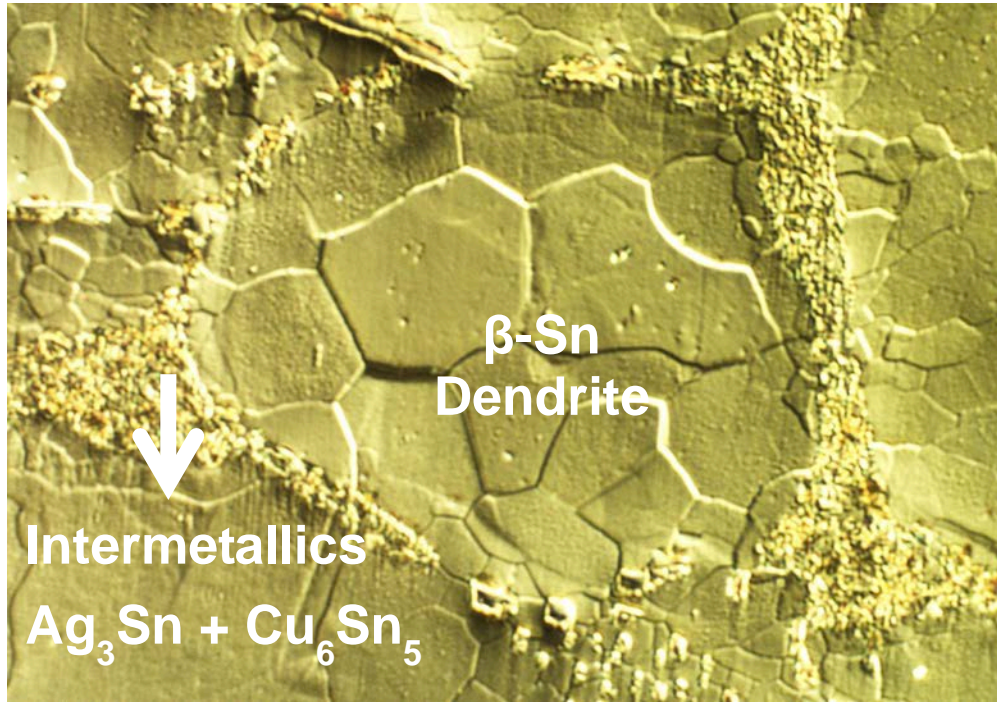
Figure 1.4 Microstructure of a β-Sn Dendrite
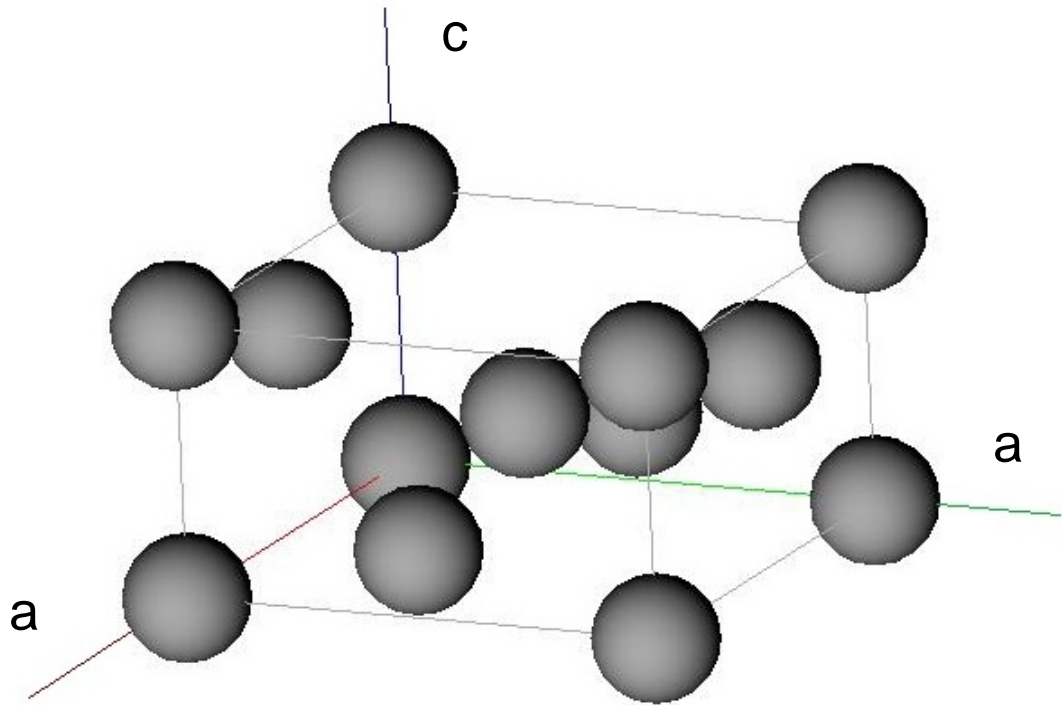
Figure 1.5 Structure of β-Sn Unit Cell

of a standard BGA solder joint was based on anisotropy of microstructure, and they developed a model to predict mechanical fatigue damage evolution. Ubachs, et al. [15] confirmed that anisotropy was correlated with the thermal fatigue life of SAC solder joints. In addition, anisotropy of β-Sn played an important part in strain distributions when solder joints were subjected to thermal loading [16]. The variations of strain in different grains lead to the development of unexpected deformations at the grain-boundary regions. Moreover, several other previous researchers pointed out that the effects of anisotropy of β-Sn should be taken into consideration as a significant factor in the development of damage and reliability modeling [17-19].

1.4   Research Objective

The main aim of this thesis is to investigate the correlation between β-Sn grain size and orientation and the mechanical behavior of SAC solder joints using the known anisotropy of β-Sn. In order to improve the theoretical prediction of the reliability properties and mechanical response on SAC solder joints in the electronic packages, the grain information will be taken into consideration and examined via Finite Element Analysis (FEA).

1.5   Thesis Organization

This thesis involves a study of the effects of grain size and orientation on the mechanical response of SAC solders. It is composed of the following chapters:

Chapter 1: Introduction to lead free solders, microstructure of SAC solders, and anisotropy of β-Sn.

Chapter 2: Literature review on effect of grain size and grain orientation on mechanical properties of SAC solders.

Chapter 3: Description of specimen preparation and experimental procedure.

Chapter 4: Quantitative measurement of sub–grain size of SAC solders using the intercept method, planimetric method, and EBSD method.

Chapter 5: Study on the effect of aging on the sub-grain size of SAC solders.

Chapter 6: Measurement and determination of grain orientations in SAC solder joints.

Chapter 7: Study of the effect of grain orientation on the mechanical response of SAC solder joints.

Chapter 8: Summary and conclusions.

CHAPTER 2

LITERATURE REVIEW

2.1   Effect of Grain Size on Mechanical Response

SAC solder joints in electronic packaging have shown variations from joint to joint in their mechanical responses. A fundamental understanding of grain structures is needed to explain and predict the mechanical behaviors of SAC solders. SAC solders with different grain sizes have different numbers of grain neighbors and grain boundary regions, thus leading to different mechanical responses such as tensile, shear, creep, and fatigue properties. Some previous studies have been conducted to measure the microstructures and grain sizes of SAC solders, and have presented explanations for observed mechanical behaviors.

Krause, et al. [20] studied the effect of solder material volume on grain sizes and grain distributions in SAC305 joints by applying the electron backscatter diffraction (EBSD) method. The technology of EBSD provides a quantitative measurement of grain sizes and orientations of solder interconnects with high spatial resolution. Nano-indentation was also used to measure the mechanical properties of the solder joints with different grain sizes. Figure 2.1 shows an EBSD mapping and arrays of nano-indents placed on regions of coarse grains with a large grain size, and areas of finer grains with a small grain size. The results of their nano-indentation tests are shown in Table 2.1. The measured data reveal higher values of hardness and elastic modulus in areas with a small
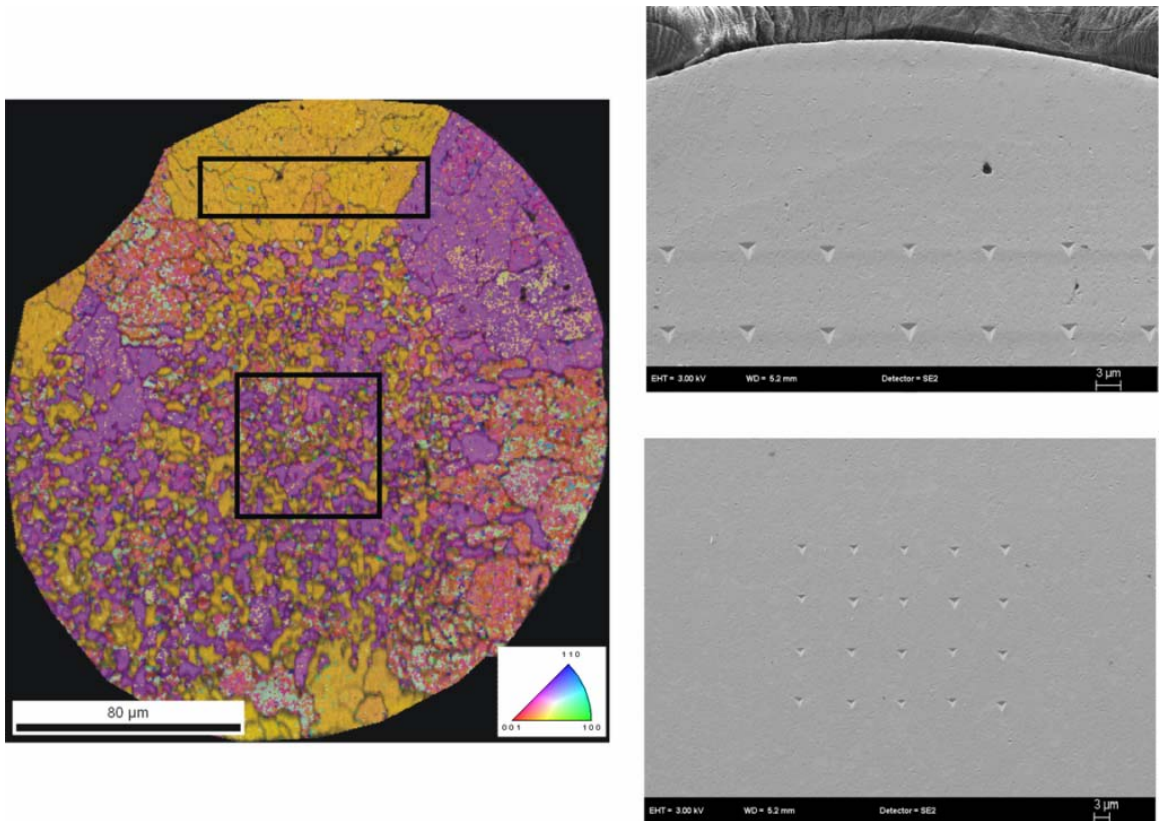
Figure 2.1 EBSD Map of SAC 305 Solder Ball and Arrays of Nano-Indents Placed in the Top and Bottom Regions [20]

	Hardness in GPa	Elastic Modulus in GPa
Large Grains	0.28	52.21
Small Grains	0.32	56.83

Table 2.1 Mean Values of Hardness and Elastic Modulus Measured in the Two Regions of a SAC 305 Solder Ball [20]

grain size compared to the values found in regions with coarse crystal grains.

Some research was also conducted to study the effect of grain size on thermo-mechanical properties [21]. SAC solder samples with multiple grains were more resistant to thermal fatigue than specimens with only a single grain. Based on this analysis of grain structures, a thermo-mechanical fatigue damage evolution model was characterized and developed to identify damage evolutions.

The above observations agreed well with the investigation by Zhang, et al. [22]. During aging, dendrites and grains in SAC solders grew larger and merged. Precipitation of Cu_6Sn_5 and Ag_3Sn intermetallics could not effectively block dislocation movement, leading to a loss of strength. This study also found that dislocation creep and grain sliding played an important role in creep deformations for solder alloys. Thus, the creep resistance in solder materials reduced when the grain size increased since Cu_6Sn_5 and Ag_3Sn intermetallic particles lost the ability to block grain boundary sliding. Furthermore, Arfaei, et al. [23] reported a similar observation for the comparison of single β-Sn grain solder balls and multi-grain solder balls. The mean shear fatigue lifetime for solder joints with multiple grains was longer than that of single grained samples, which confirmed the mechanism of dislocation for solders with different grain sizes.

As demonstrated above, the effect of aging time on SAC solder alloys or solder joints has been regarded as one of predominant factors for the determination of grain size, which thus influences mechanical responses. Xiao, et al. [24] investigated the tensile behavior of SAC396 alloys during room temperature aging. The grain size of β-Sn had coarsened after 35 days of aging at room temperature, as shown in Figure 2.2. Correlating
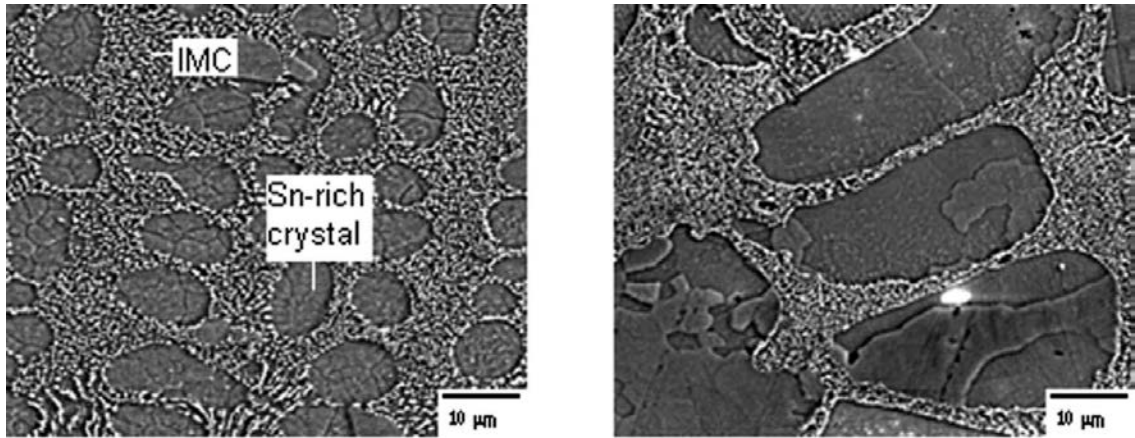
(a) as quenched

(b) 35 days RT
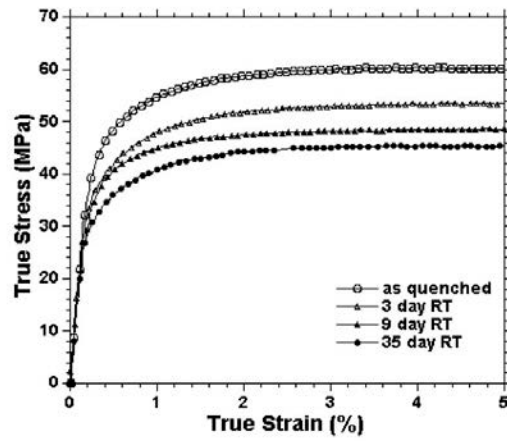
(c) aging at RT

Figure 2.2 Backscattered Electron Images and Tensile Behaviors of As-Quenched and Room Temperature Aged SAC396 Alloys [24]

with the change of the microstructure and β-Sn grain growth, the alloy became softer, decreasing ultimate tensile strength by 25% from 60 MPa to 45 MPa as room temperature aging time increased up to 35 days.

Ma, et al. [25] also reported on the effects of room temperature aging on the mechanical properties (elastic modulus, yield stress, ultimate strength, and creep compliance) of SAC405 and SAC305 specimens. Stress-strain, creep tests, and microstructure studies were performed on the aged solder materials, and the mechanical properties of the alloys were modeled as a function of aging time at room temperature. The ultimate tensile strength of SAC405 specimens decreased by up to 40% after 63 days of room temperature aging. The stress-strain behavior of the alloys degraded most dramatically during the first 10 days of room temperature aging. The initial linear behavior of SAC samples in the stress-strain curves changed less than the post yield behavior during room temperature aging. The observed microstructure evolution correlated with the degradations of mechanical properties of SAC specimens. Grains and dendrites grew larger, and the Ag_3Sn and Cu_6Sn_5 intermetallics congregated around the dendrites, which caused the ultimate tensile strength reduction.

Increases in aging temperature and/or aging time have been found to exacerbate the aging effect, and lead to larger changes in grain structures and mechanical responses of lead free solder materials. Cai, et al. [26] presented a parallel study of microstructure evolutions of Sn-0.3Ag-0.7Cu-0.1Bi (SACX0307) solders aged at various temperatures, as shown in Figure 2.3. Faster evolution of the microstructure of the SACX0307 solder was seen for elevated temperature (T = 125 ºC) aging compared to room temperature (T

SACX0307, RF, Aged at 25 ^{o}C (SEM, 250X)
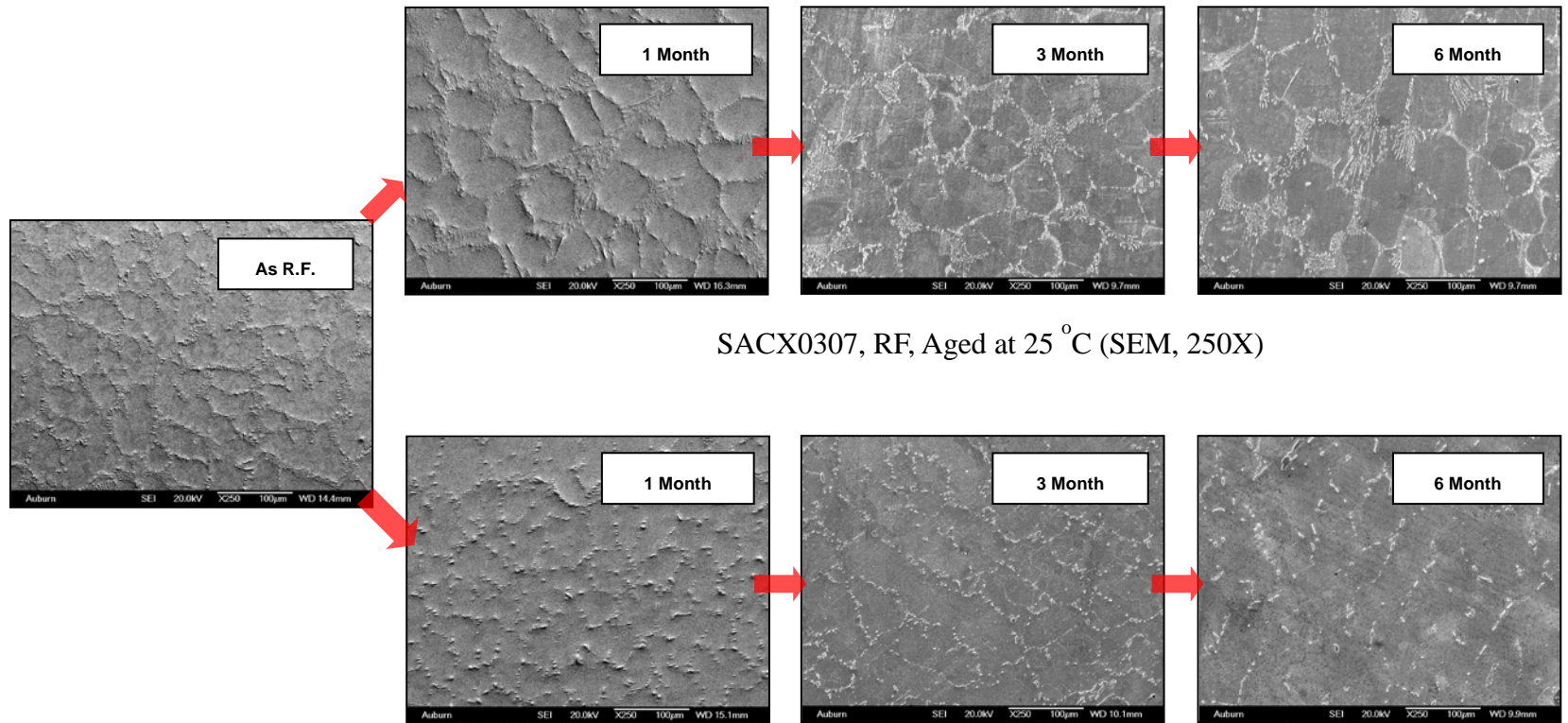
Figure 2.3 Microstructure Evolution of SACX0307 under Different Aging Conditions [26]

SACX0307, RF, Aged at 125 ^{o}C (SEM, 250X)

= 25 $^{\circ}$C) aging. The degradation of mechanical behavior was also explained from the investigation of microstructures of solder samples subjected to various aging conditions.

2.2   Effect of Grain Orientation on Mechanical Response

Due to the anisotropic nature of the lattice structure of β-Sn, mechanical behaviors of SAC solders that contain a high percentage of β-Sn are also influenced by grain orientations, and mechanical properties are anisotropic with respect to crystal directions. Figure 2.4 illustrates that the theoretical elastic modulus of β-Sn varies with the orientation of grains, ranging from 23.6 GPa to 64.4 GPa, which might lead to variation of the elastic modulus of solder materials [27, 28]. Zamiri, et al. [29] also confirmed that differences of grain orientation led to solders exhibiting different mechanical properties. Figure 2.5 shows uniaxial stress–strain behavior of two hardening models for three different crystal orientations: along the a axis, along the c axis, and 45° from the a and c axes. These results demonstrate the grain orientation has a significant effect on stresses and strains in the solder joints.

Traditionally there are several methods employed to study the grain orientation of materials, such as EBSD, X-ray diffraction (XRD), neutron diffraction, polarized light microscopy, and TEM diffraction. In polarized light images, different crystal orientations can be distinguished by different colors, but this method does not provide a quantitative measurement of the crystal orientations. Therefore, the XRD and EBSD methods are usually chosen to characterize the crystal structures with more quantitative information on the crystallographic orientation. Song, et al. [30] combined the XRD and EBSD methods to investigate grain orientations of the intermetallic compound Cu_6Sn_5 formed at

18
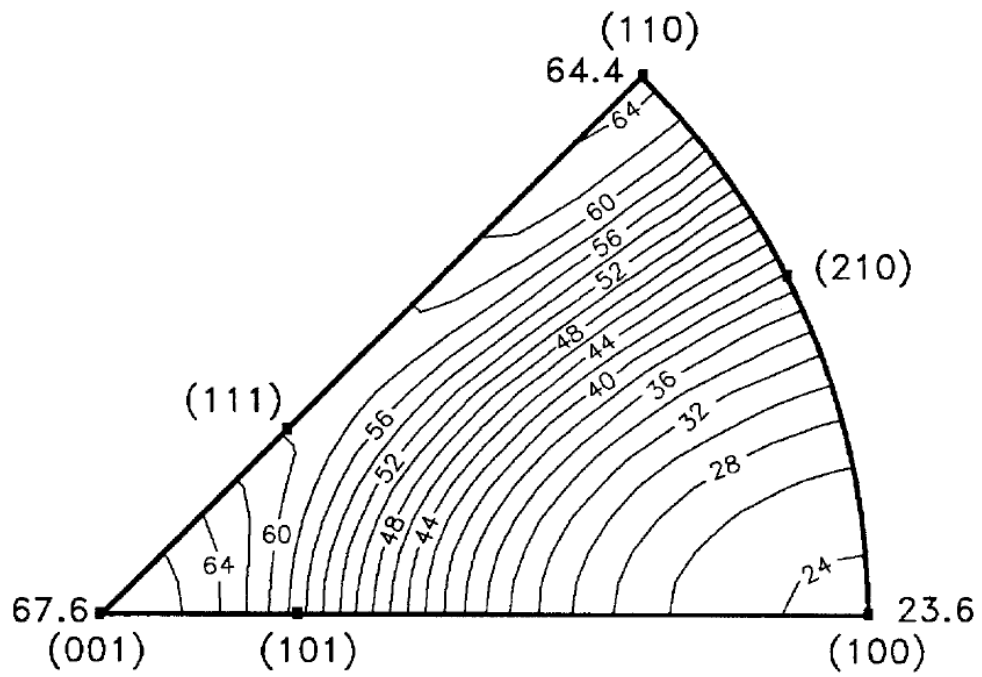
Figure 2.4 Calculated Elastic Moduli of β-Sn (GPa) [28]
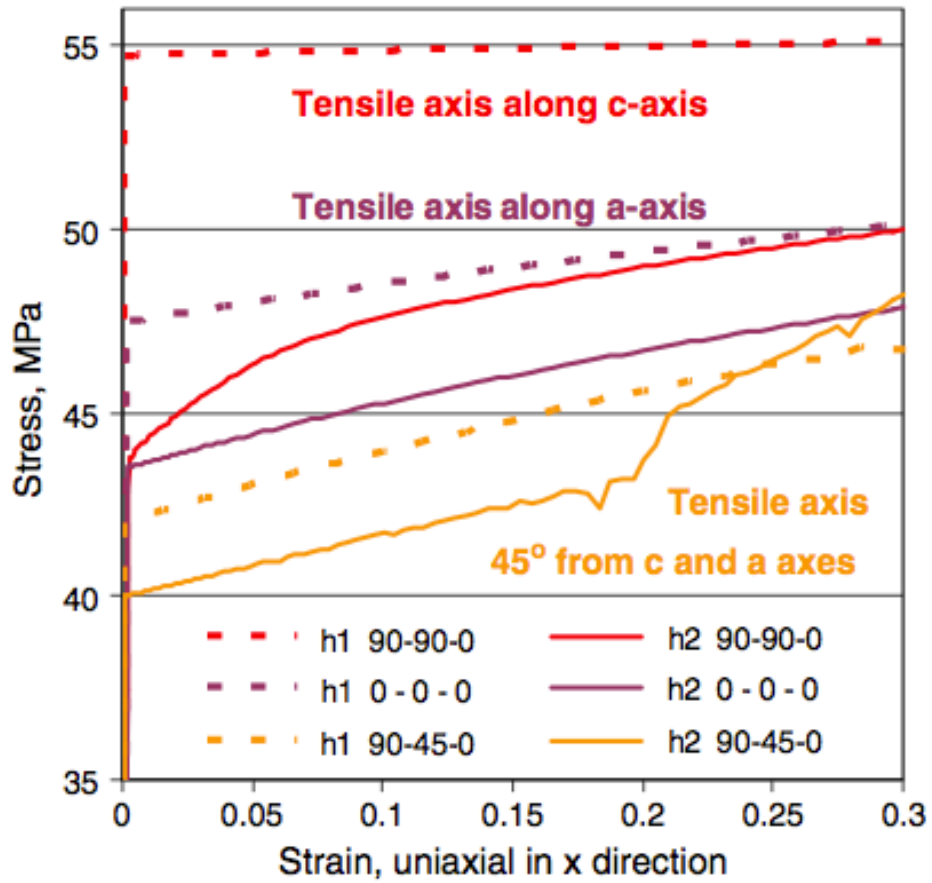
Figure 2.5 Uniaxial Stress–Strain Curves for Two Hardening Models [29]

the interface of SAC solder joints. By analyzing the XRD pattern, crystal orientations were revealed by diffraction peaks. However, the XRD technique can only give the overall textural information and the average orientation over an area of samples illuminated by the X-ray beam [31]. The EBSD technique has the advantage of scanning multiple grains in solder materials and obtaining individual orientation information, instead of the bulk crystal orientation. Also, the EBSD method can measure materials with two or more different phases, and analyze each grain size and grain orientation of the materials from the pole figures or inverse pole figures. Therefore, the EBSD method more commonly used to determine the grain orientations of solder materials.

Bieler, et al. [32] performed EBSD crystal direction maps on eleven joints from a row in a thermo-mechanically cycled PBGA package, as shown in Figure 2.6. This study showed a variety of grain orientations, which caused non-uniform stress distributions from joint to joint. For the solder balls in the orange color with c axis parallel to pad surface, cracks happened and propagated after thermal cycling, which illustrated a clear correlation between the damage in solder balls with the β-Sn grain orientation.

Nano-indentation tests are routinely conducted to measure the hardness, yield strength, and elastic modulus of SAC solders. The combination of the nano-indentation measurements and the EBSD method provides a better understanding of the relationship between grain orientations and mechanical behaviors. Juergen, et al. [33] compared the hardness found using nano-indentation measurements with the crystal orientation obtained using EBSD measurements. The results indicated solder joints with different grain orientations had different hardness values and reliability data.
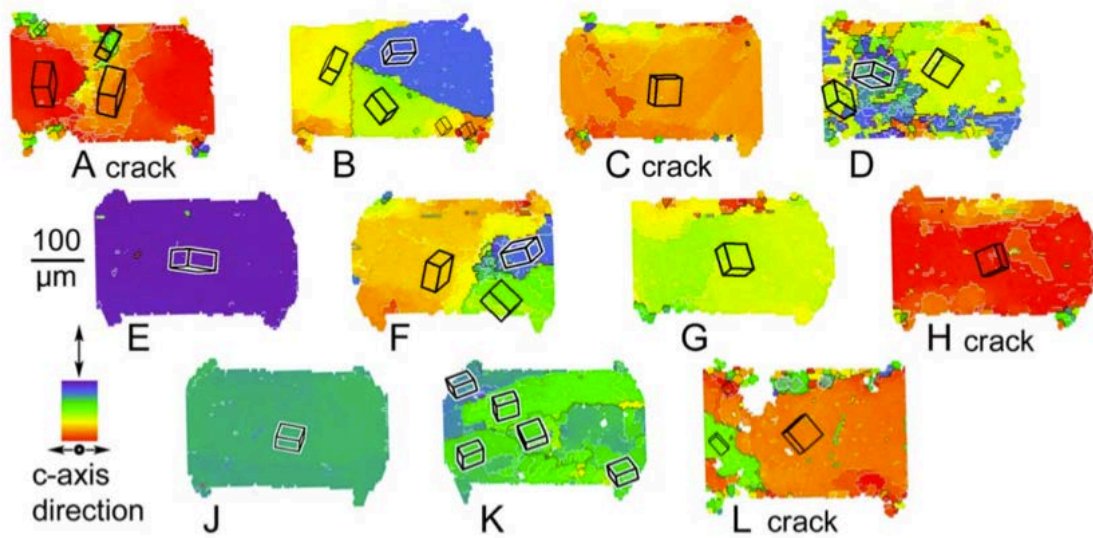
Figure 2.6 Crystal Direction Maps of Eleven Joints from a Row in a Package [32]

2.3   Summary and Discussion

In this chapter, a review was performed on the effect of grain sizes and grain orientations on mechanical responses of SAC solders. SAC solders typically contain a high percentage of β-Sn, and cannot be regarded as homogenous, isotropic materials because of the anisotropy of the intrinsic tetragonal β-Sn matrix. Numerous research papers have already demonstrated that the increase of grain sizes, or the grain growth induced by aging, can result in a reduction in elastic modulus, hardness, creep resistance, shear fatigue lifetime, and thermo-mechanical properties. Also, the EBSD method and nano-indentation measurements have been widely developed and used for determining grain orientations, elastic modulus, yield strength, and hardness. Thus, grain orientations must be taken into consideration for complete understanding of the mechanical behaviors of SAC solders.

.

CHAPTER 3

SPECIMEN PREPARATION AND EXPERIMENTAL PROCEDURES

3.1   Bulk Specimen Preparation Procedure

In this chapter, a preparation procedure for bulk uniaxial test specimens of solder alloys is presented. Compared with real solder joints in electronic packaging, bulk specimens have more uniform microstructures and multiple β-Sn grains, resulting in more uniform mechanical properties.

The setup for the procedure is shown in Figure 3.1. The solder alloy is melted in a crucible with a pair of heating coils, and thermal couples are attached to the crucible to control the temperature. One end of a rectangular cross-section glass tube is inserted into the molten solder, and the other end provides a suction force by using a vacuum pump. A regulator on the vacuum system controls the force drawing the solder into the tube. The bulk uniaxial specimen is typically formed with dimensions of 80 x 3 x 0.5 mm. Then, the glass tubes are cooled by water quenching or more slowly using a controlled reflowed oven with different temperature versus time profiles, as illustrated in Figure 3.2 and Figure 3.3. Finally the glass tube is removed (Figure 3.4), and the bulk specimen is inspected by a micro-focus X-ray system to detect its quality. Figure 3.5 shows an example of good and bad specimens. Samples without notches, voids, and other flaws were used in this study.
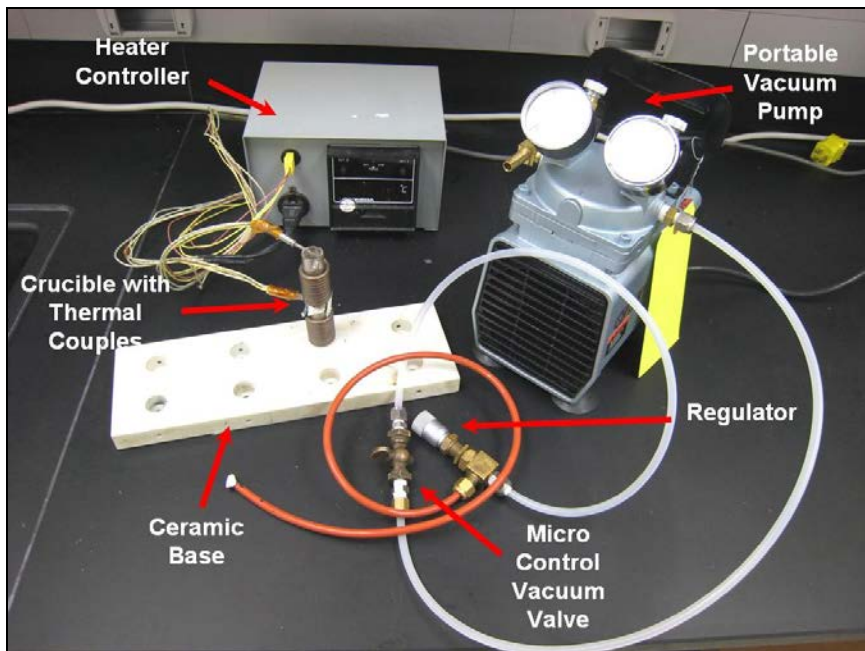
Figure 3.1 Setup for Bulk Specimen Preparation
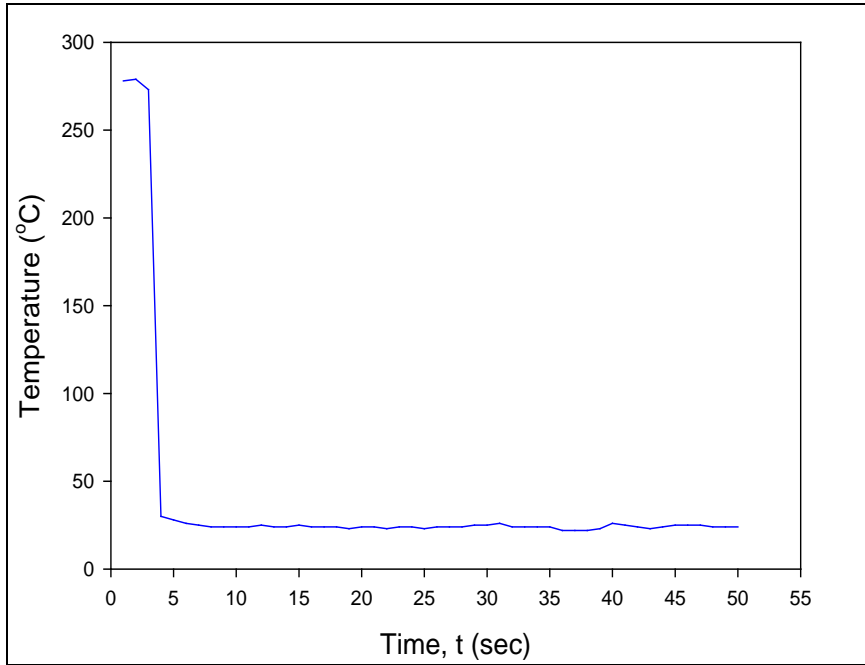
Figure 3.2 Solder Water Quenching Temperature Profile
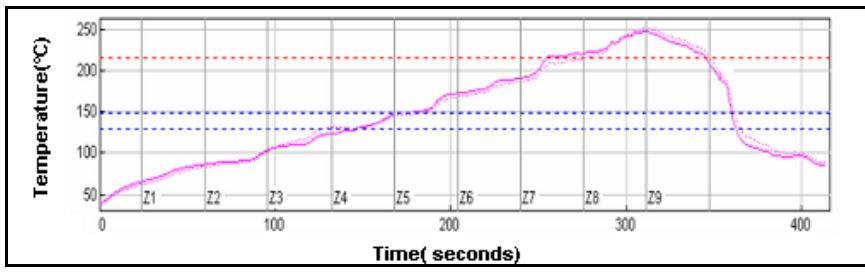
Figure 3.3 Solder Reflow Temperature Profile

26

(a) Sample with Glass Tube

(b) Sample without Glass Tube

Figure 3.4 Solder Bulk Specimens
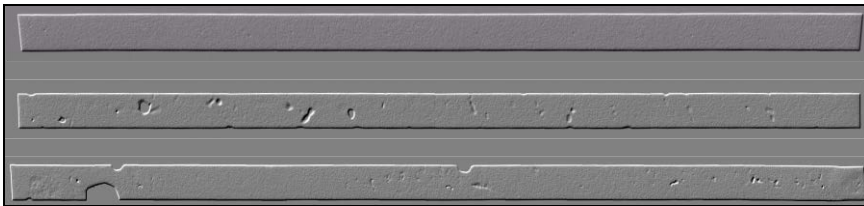
Figure 3.5 X-Ray Inspection of Bulk Specimens

3.2   Sectioning, Mounting, and Polishing Procedure

For microscopy studies, the bulk specimen or electronic package was cut into a proper length, and then the sample was cut again to reveal the cross-section of interest. The sample was then mounted in a prepared conductive epoxy resin stub. Silicon carbide (SiC) sand papers with grit sizes of 320, 600, and 1200 were used to grind and polish the cross-sectioned bulk specimen or package. The polishing process was performed on a metallographic rotating disk, as shown in Figure 3.6. Fine polishing was then conducted on a porous neoprene cloth, adding 0.05-μm-particle-size BUEHLER MasterPrep alumina polishing suspension. Finally, the surface of the sample was cleaned with distilled water and compressed air. If sub-grain structures needed to be investigated, a chemical etchant mixture of 5% hydrochloride and 95% methanol was used to etch the sample surface for 2-10 seconds.

3.3   Microstructure Investigation

An OLYMPUS BX60 optical microscope equipped with a Nomarski prism was used to analyze the microstructures of the bulk solder alloys and solder joints in cross-sectioned packages, as shown in Figure 3.7. Polarized light images were taken by adjusting the polarization filters to identify different grains in the samples. A JEOL JSM-7000F Field Emission Scanning Electron Microscope (SEM) (see Figure 3.8) was also utilized for revealing morphology of bulk solder alloys or solder joints. The grain or sub-grain orientation was characterized by an EBSD system (HKL, channel 5) attached to the JEOL JSM-7000F SEM instrument equipped with a field emission gun. The utilized Nordlys II EBSD Detector is displayed in Figure 3.9.
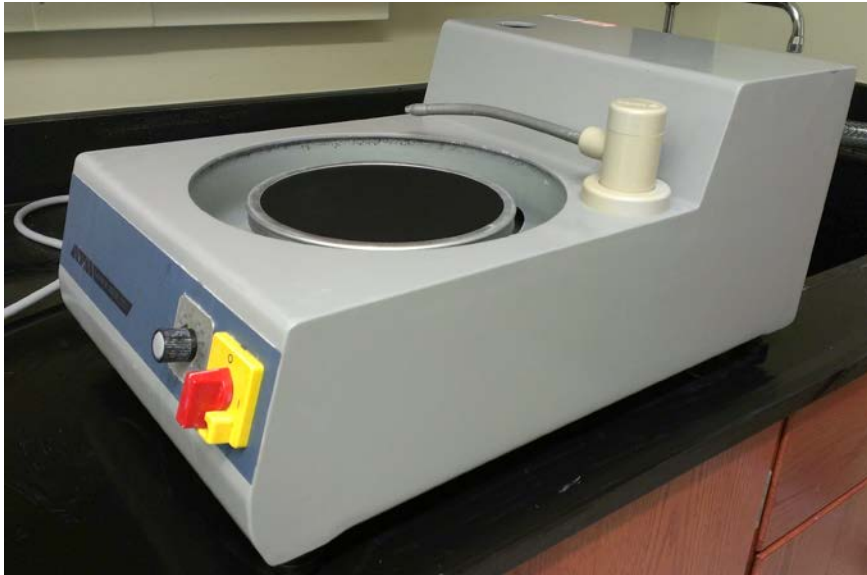
Figure 3.6 Microscopy Sample Polishing Machine

Figure 3.7 OLYMPUS BX60 Optical Microscope

Figure 3.8 JEOL JSM-7000F Field Emission SEM
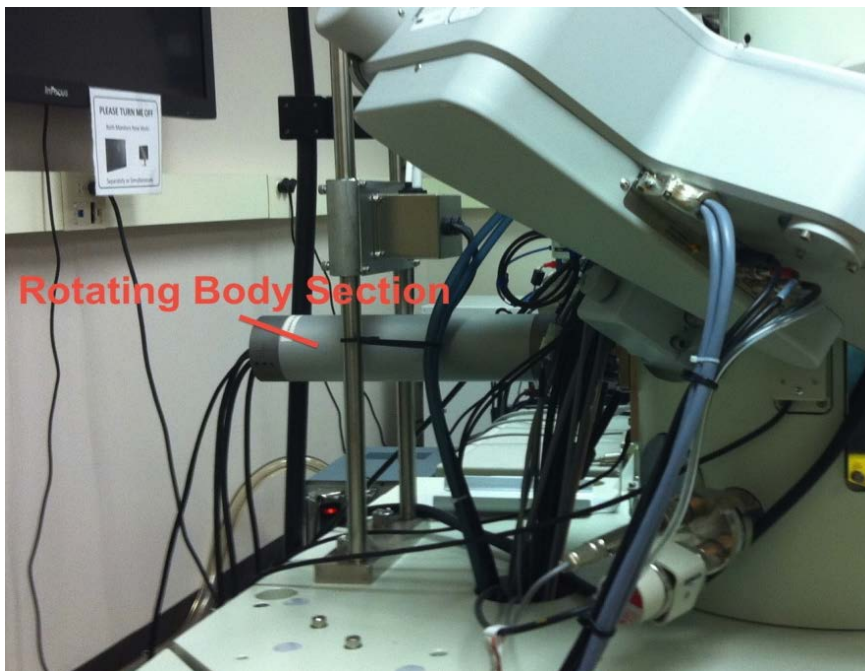
Figure 3.9 Nordlys II EBSD Detector

CHAPTER 4

QUANTITATIVE MEASUREMENT OF SUBGRAIN SIZE
OF LEAD FREE SOLDER ALLOYS

4.1   Intercept Method

According to ASTM Standard E 112-96 [34], the intercept method was used to quantitatively measure sub-grain sizes of lead free solder alloys. Several optical images of Sn-0.3Ag-0.7Cu-0.1Bi (SACX) bulk solder samples were taken by an OLYMPUS BX60 optical microscope. One dendrite or a certain area was chosen to draw several test lines across the field of the image with a certain meshing, as shown in Figure 4.1. The mean lineal intercept length (L) was calculated by counting sub-grain boundary intersection that the test lines cut across. The results are listed in Table 4.1. The ASTM grain size number (G), which is defined as: $N_{AE}=2G-1$, where N_{AE} is the number per square inch at 100X magnification, can be obtained by the following equation:

$$G = (-6.643856 \log_{10} L) - 3.288 \tag{4.1}$$

where L is intercept length in mm.

A smaller G represents a larger grain size in a certain area. Comparing different mesh densities in Figure 4.1, the 5 x 5 meshing was not adequate enough to measure the average grain size. The results converged for finer meshing such as 10 x 10, 15 x 15, and 20 x 20 meshing.

5 x 5
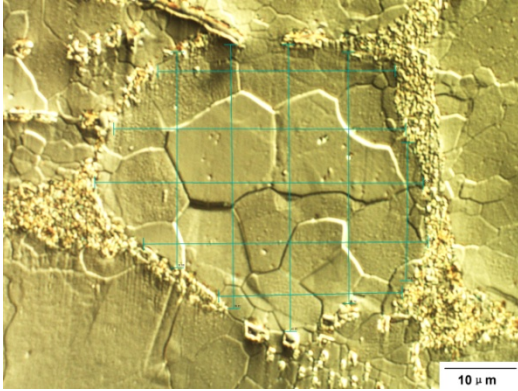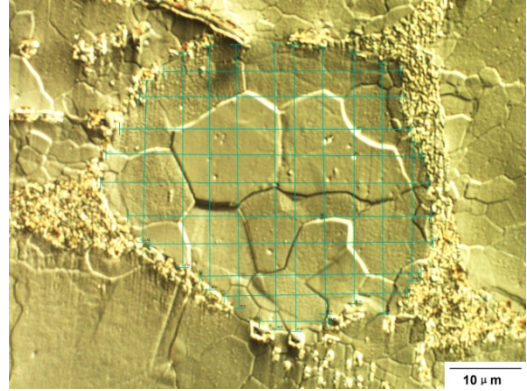
10 x 10
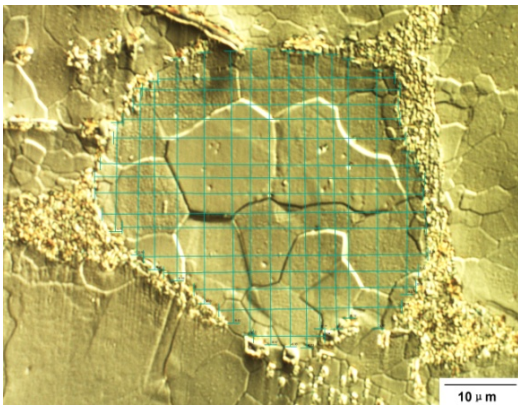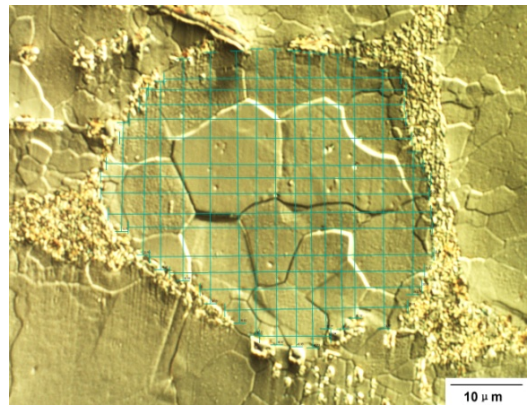
15 x 15

20 x 20

Figure 4.1 Optical Images of SACX Solder with 5 x 5, 10 x 10, 15 x 15, and 20 x 20

Meshing

Meshing	5 x 5	10 x 10	15 x 15	20 x 20
L (µm)	9.43	9.17	9.11	9.13

Table 4.1 Calculation of Mean Lineal Intercept Length L

4.2   Planimetric Method

The planimetric method described in ASTM Standard E 112-96 can also be used for measuring sub-grain sizes of lead free solder alloys. Instead of counting the intercept length L, the number of grains per unit area N_A is considered. A grain inside of the area is counted as one grain, while grains crossing the boundaries of the area are counted as one half grain. The average grain area (A) can be written as

$$A = \frac{1}{N_A} \tag{4.2}$$

where N_A is in mm^{-2}, and the ASTM Grain Size Number G is expressed by

$$G = (3.321928 \log_{10} L) - 2.954 \tag{4.3}$$

Figure 4.2 shows an example of the planimetric method. An area of 20 x 20 μm^2 was chosen to draw 10 x 10 lines. The average grain area A was calculated as 44.4 μm^2, and therefore G was 11.52.

4.3   Electron Backscatter Diffraction (EBSD) Method

4.3.1   EBSD Setup and Procedure

Electron Backscatter Diffraction (EBSD) is a technique that is commonly used to characterize crystallographic properties such as grain sizes and grain orientations on the surface of specimens. An EBSD system (HKL, channel 5) attached to a JEOL JSM-7000F SEM was used in this work. As illustrated in Figure 4.3, the specimen is tilted at 70° from the horizontal position in the SEM chamber to obtain the strike of electrons. Electrons from the sample scatter and travel in all conceivable directions. They reach the
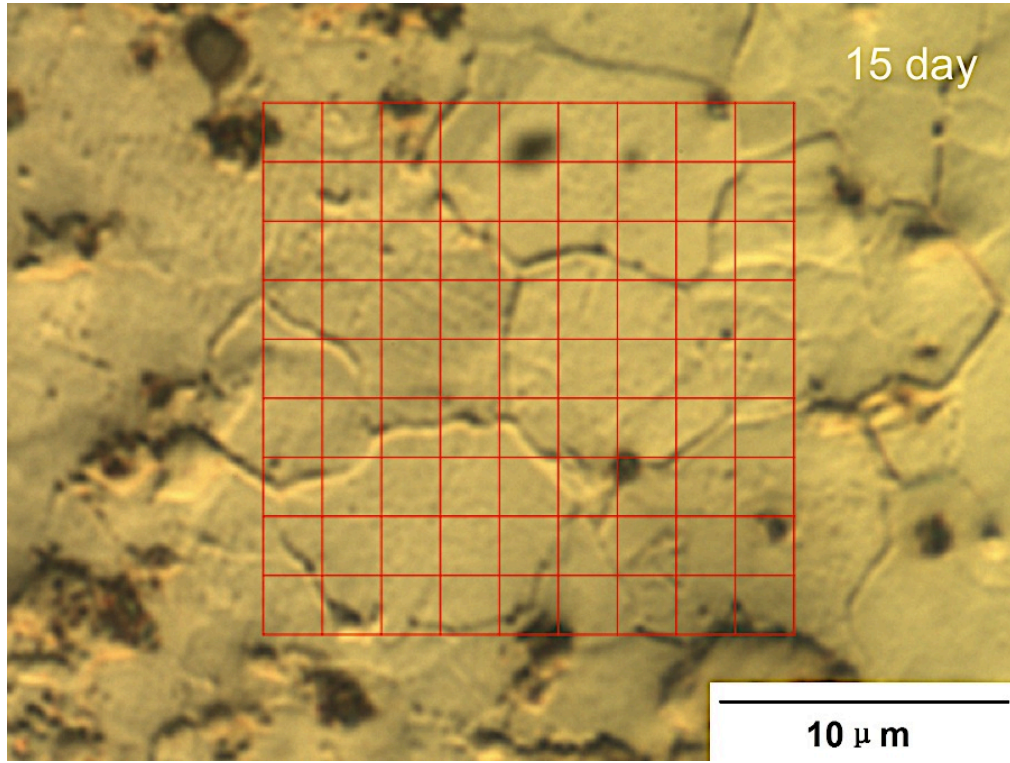
Figure 4.2 Planimetric Method Applied to Optical Image of SACX after 15 Days Aging

at 125 ºC
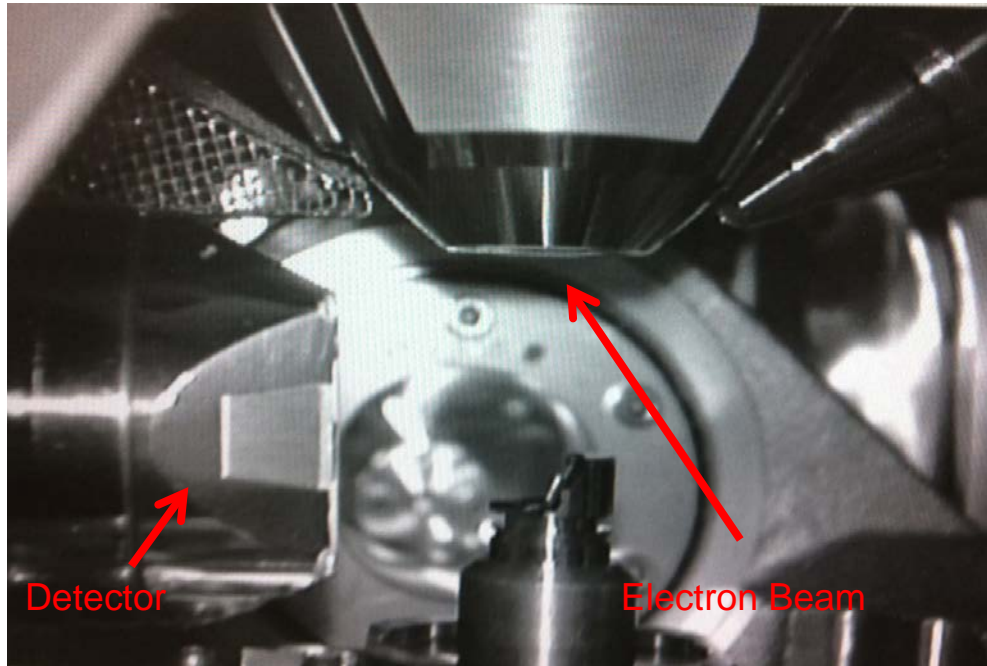
(a) Principal Components in EDBS System

(b) Sample Holder

Figure 4.3 Setup for EBSD System

detector and form the so-called Electron Backscatter Diffraction Pattern (EBSP). If the tilting angle is larger than 70°, the strength of the EBSP will increase, and the charging effect will reduce. However, the effect of surface roughness or dirt particles will also increase, which leads to poor resolution. If the tilting angle is smaller than 70°, the effect of surface roughness will reduce and the resolution will improve. However, the EBSP signal will also become weak.

Electrons satisfy the Bragg law [35]:

$$n\lambda = 2d\sin\theta \qquad (4.4)$$

where λ is the wavelength of the incident beam, n is the order of the diffraction process, d is the interplanar spacing, and θ is the Bragg angle. The wavelength (λ) of electrons is about 0.0086 nm when the accelerating voltage in SEM is 20 kV. For a particular crystallographic plane, these scattered electrons form two cones and intersect the screen of the detector, which generate straight lines of so-called Kikuchi bands. Sets of crystallographic planes form several intersecting Kikuchi bands on the phosphor screen. From an available phase database of EBSD results for β-Sn, the collected EBSP or Kikuchi bands can be indexed, as shown in Figure 4.4. After analyzing the EBSP, an area of the specimen surface is chosen to do automated mapping. Finally, collected EBSD data can be analyzed in the post processing to determine grain sizes and orientations using the software such as Tango and Mambo. Tango is used for a wide variety of maps to measure grains. Mambo is used to produce pole figures and inverse pole figures from EBSD orientation data. The primary steps of the EBSD method are given in Figure 4.5.
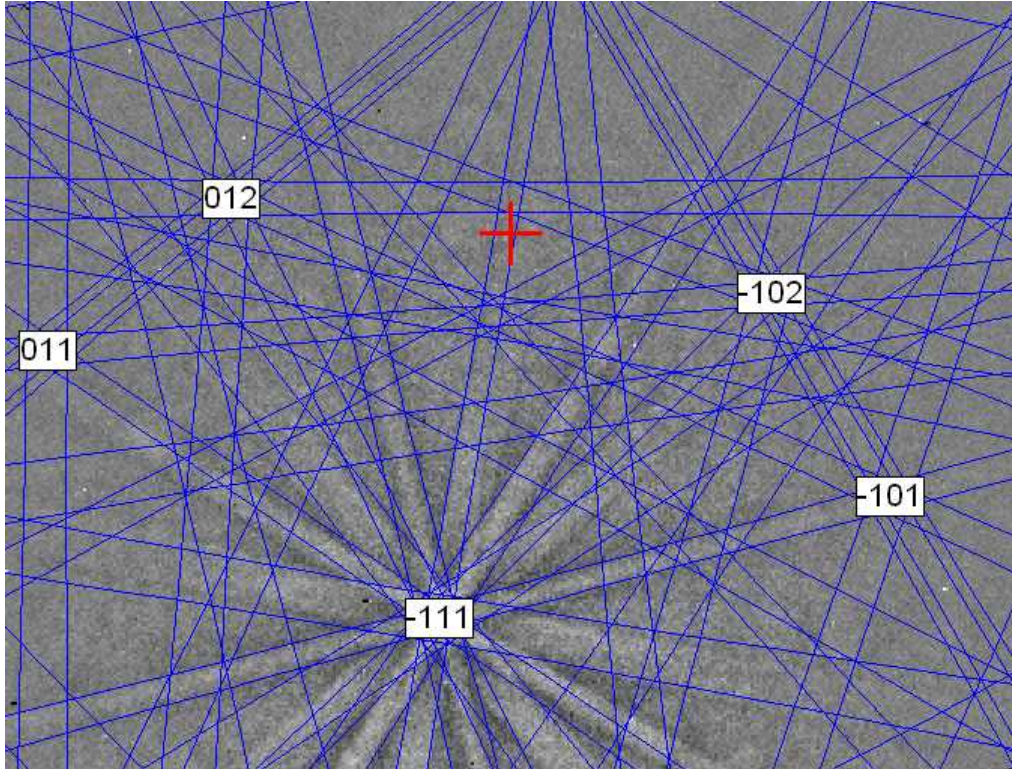
Figure 4.4 Detection of Kikuchi Band

Position Beam
Acquire SEM Image

Snap EBSP

Index EBSP

Tango

Mambo

Post Processing Data

Collecting Data

Store Phase and Orientation
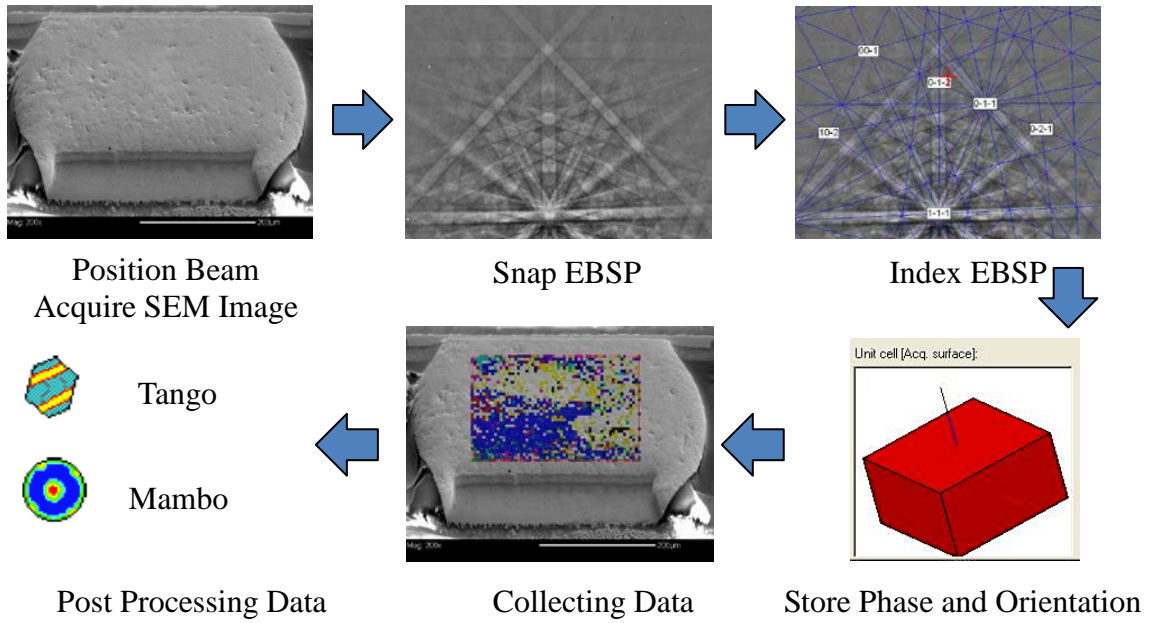
Figure 4.5 Primary Steps of the EBSD Method

4.3.2 EBSD Results and Post Analysis

Example EBSD mapping results for one dendrite in a SAC 105 solder sample is shown in Figure 4.6. Here, only the β-Sn phase without IMC is indexed from the database due to the high weight percentage of β-Sn in this lead free solder alloy. The utilized step size was 1 μm. Based on the mapping data, Tango calculated each sub-grain area scanned and obtained the average value of 55.5 $μm^2$. Compared to the automated measurement of EBSD, the intercept method and planimetric method were also used to manually measure the sub-grain size by choosing the same area of the specimen and drawing 10 x 10 lines, as shown in Figure 4.7. The results show a good agreement with sub-grain size characterized by EBSD, as shown in Table 4.2. When comparing the three measurements, the results of planimetric method agree with the results of the EBSD method, since they are both based on the grain area measurement.

4.4 Summary and Discussion

In this chapter, sub-grain sizes were quantitatively measured by ASTM standard E112-96 based intercept method, the planimetric method, and the EBSD method. An Optical microscope, SEM, and EBSD system were used. For the manual measurement, the results of the average sub-grain size converged when increasing the mesh density. 10 x 10 or finer meshing was necessary for accurate determination of the grain size. When comparing the three methods, the grain size calculation from the planimetric method was closer to that of the EBSD method.
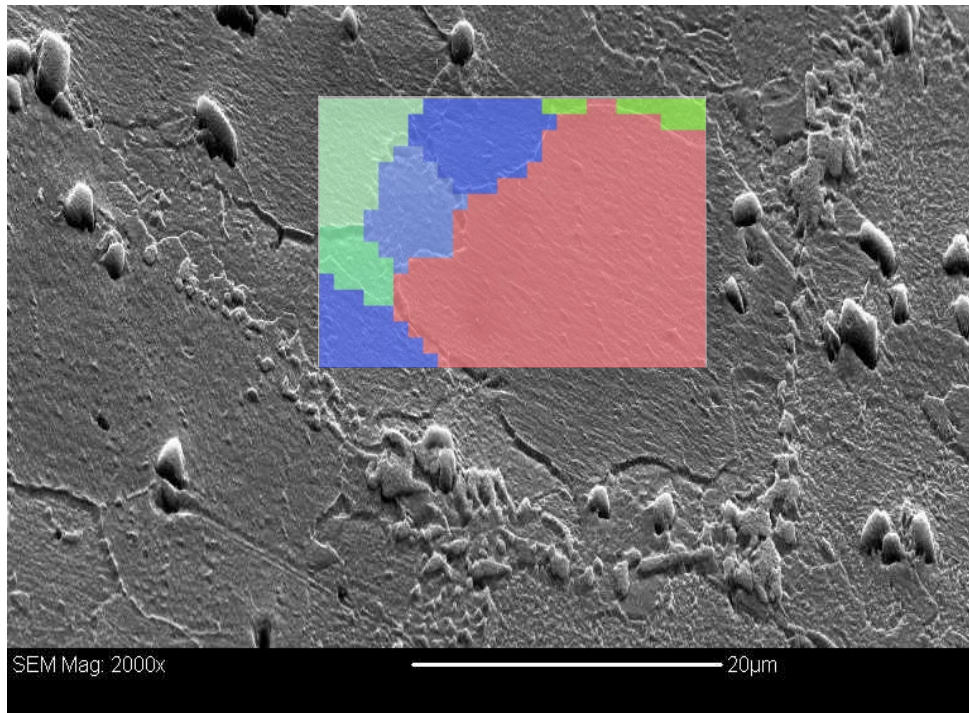
Figure 4.6 Example OIM Map for SAC 105 Solder Alloy
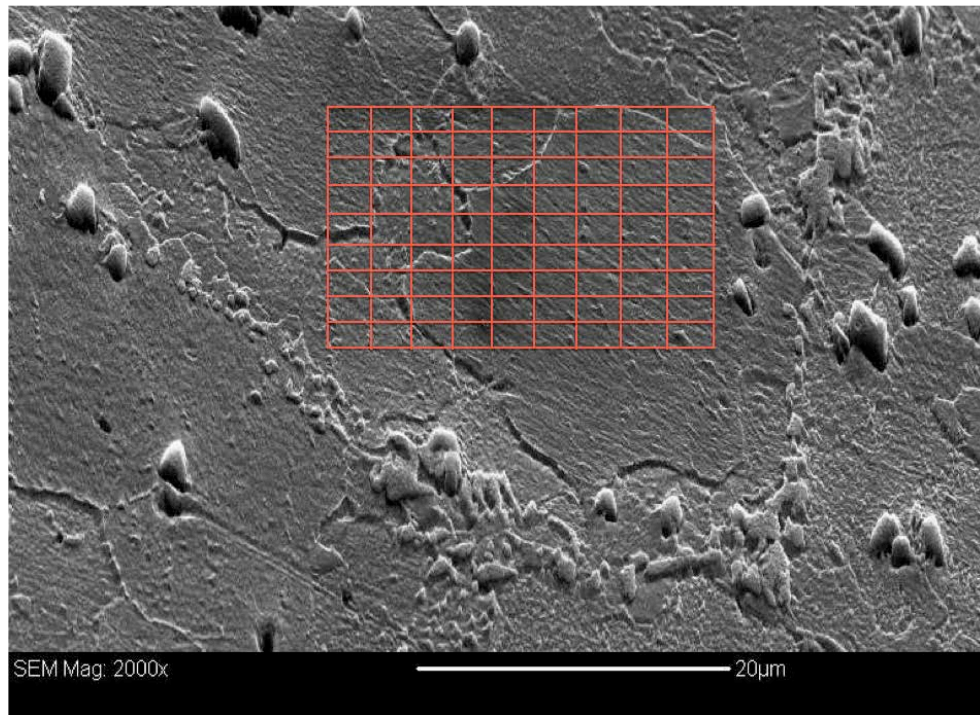
Figure 4.7 ASTM Standard E 112-96 Measurements for SAC 105 Solder Alloy

	Mean Intercept Length L (µm)	Average Grain Area A (µm^2)	Grain Size Number G
Intercept Method	10.2	X	9.94
Planimetric Method	X	57.2	11.1
EBSD Method	X	55.5	11.2

Table 4.2 Comparison of Three Methods for SAC 105 Solder Alloys

CHAPTER 5

EFFECT OF AGING ON SUB-GRAIN SIZE
OF LEAD FREE SOLDER ALLOYS

5.1 Effect of Aging Time on Sub-grain Size

Solder interconnects are often exposed to isothermal aging conditions. In this chapter, the effect of aging time was examined by measuring the sub-grain sizes.

As discussed in the previous chapters, the planimetric method can be used to measure the average grain size in SAC solder alloys. Optical images of SACX samples subjected to aging at 125 °C were taken by an OLYMPUS BX60 optical microscope to investigate the effect of aging time on sub-grains using the planimetric method, and 10 x 10 meshing. Appendix I shows the observed microstructure evolution during aging, including β-Sn phase coarsening, accumulation of IMC particles, and sub-grain growth in SACX alloys.

The evolution of sub-grain size with aging time can be fit with the relationship proposed by Allen, et al. [36],

$$D^n - D_0^n = K_0 t \exp(\frac{-Q}{RT})$$ (5.1)

where D is the mean linear intercept size of the grains (which is same as the mean intercept length L in Chapter 4) at aging time t, D_0 is the mean linear intercept size of the grains at aging time t = 0, n is the exponent of grain size (n ≥ 2), K_0 is a material constant which is not dependent on aging time or temperature, Q is the activation energy for the

coarsening process, R is the gas constant, and T is the absolute temperature of aging. Since the aging temperature remained constant at 125 °C, Eq. 5.1 can be simplified to:

$$D^n - D_0^n = Kt \tag{5.2}$$

where $K = K_0 \exp(\frac{-Q}{RT})$. The model fitting and the experimental measurements based on the planimetric method are plotted in Figure 5.1, where $D_0 = 4.17$ μm, n = 5.274, and K = 2824.

The tendency of the sub-grain size to increase during aging can be explained by the fact that sub-grains will combine together to reduce the grain boundary energy when aging time increases. As presented in Chapter 2, it was reported that an increase of grain sizes or the grain growth leads to a degradation of the mechanical properties. Therefore, the mechanical properties will decrease during aging. Also, Figure 5.1 indicates that the sub-grain size increases dramatically in the first several days, which correlates well with the mechanical property degradations observation by Cai, et al. [37]. In that work, the mechanical properties such as elastic modulus, yield stress, and ultimate strength of solder alloys were found to degrade more quickly with aging during the initial aging period.
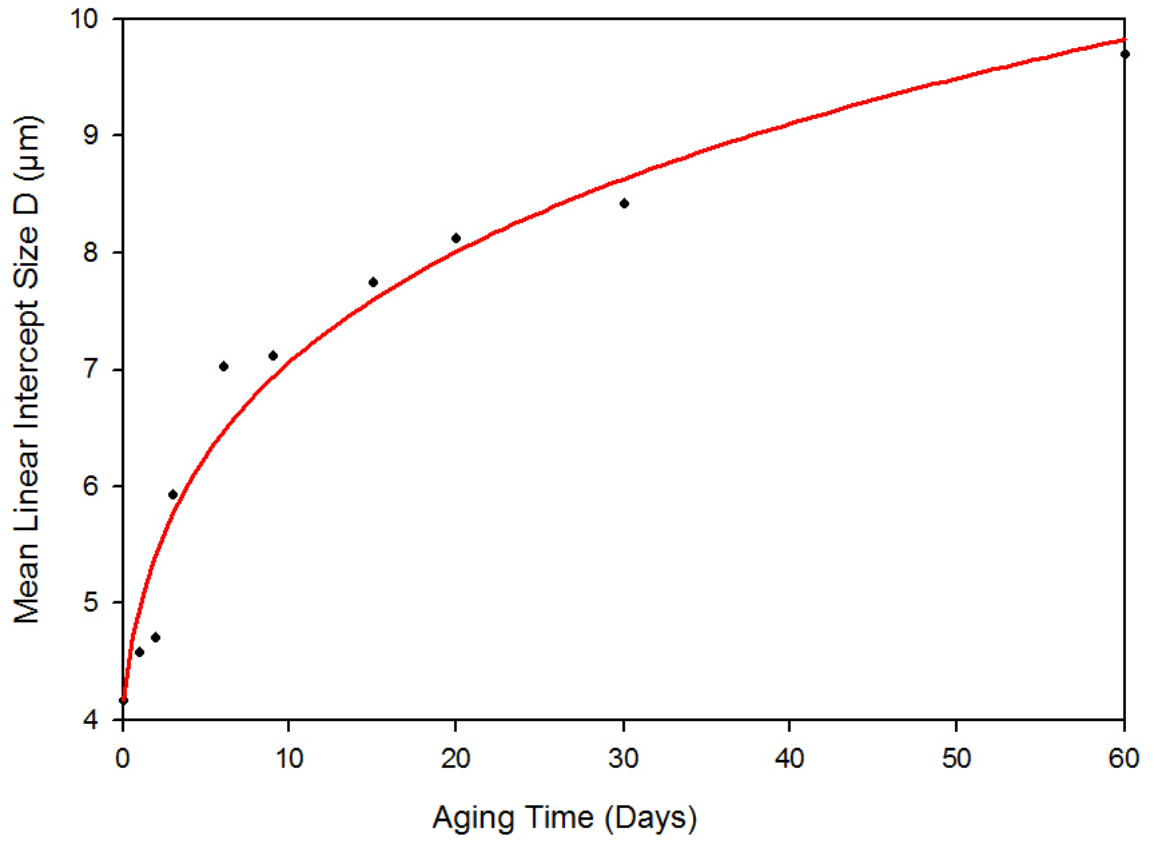
Figure 5.1 Increase in Sub-grain Size with Aging for SACX

5.2   Effect of Aging Temperature on Sub-grain Size

The effect of aging temperature was also examined by analyzing the sub-grain size using the intercept method and 20 x 20 meshing. SACX solder alloy was examined for aging of one month at 25 $^{\circ}$C and one month of 125 $^{\circ}$C. Figure 5.2 indicates that the sub-grains grew faster when increasing the temperature of aging. Three different dendrites for each condition were chosen to obtain the average value of L, as illustrated in Appendix II. The results shown in Table 5.1 indicate the convergence of L when increasing the mesh density. Finer meshing, such as a 20 x 20 meshing, is recommended. Figure 5.3 shows the aging temperature has a strong effect on the sub-grain size growth in the three dendrites, with higher aging temperature accelerating the aging effect.

5.3   Summary and Discussion

In this chapter, the effects of aging time and aging temperature were examined based on the measurement of sub-grain sizes. SACX solder alloys were used for aging under different conditions. It has been shown that the sub-grain size is sensitive to aging, increasing with aging time. In addition, increased aging temperature caused increased sub-grain growth. Moreover, since the sub-grain size is correlated to mechanical properties such as elastic modulus, yield stress, and ultimate strength, the effect of aging time and temperature can influence the mechanical response of solder alloys as well.
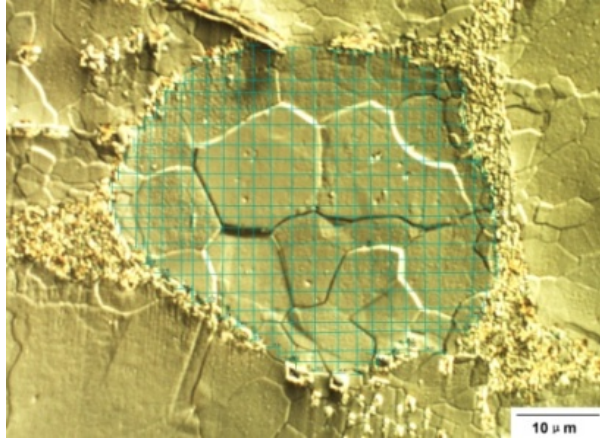
(a) SACX with No Aging (20 x 20 Meshing)
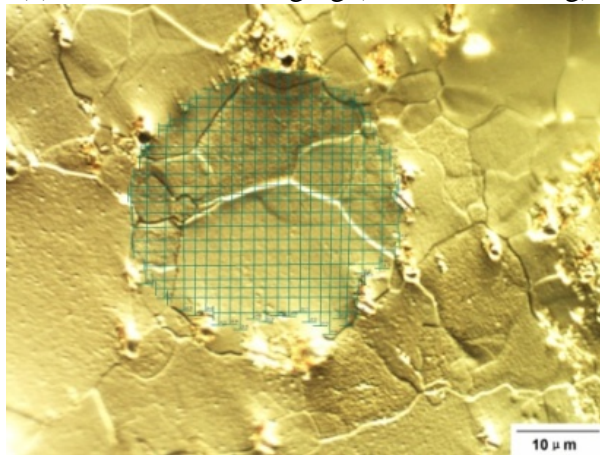
(b) SACX with 1 Month Aging at 25 $^{\circ}$C (20 x 20 Meshing)
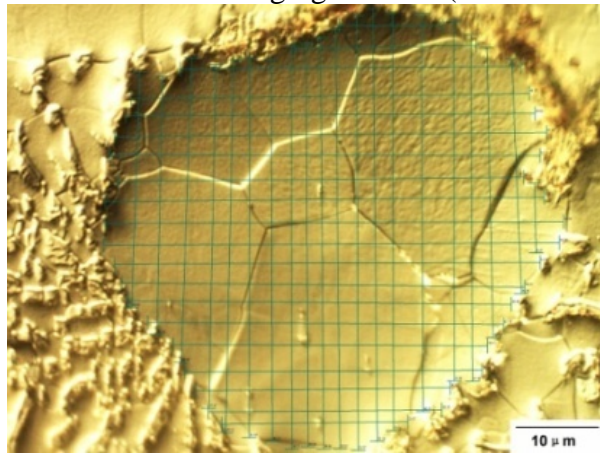
(c) SACX with 1 Month Aging at 125 $^{\circ}$C (20 x 20 Meshing)

Figure 5.2 Sub-grain Size Evolution of SACX with No Aging, 1 Month Aging at 25 $^{\circ}$C,

and 1 Month Aging at 125 $^{\circ}$C

	Dendrite 1				Dendrite 2				Dendrite 3				L (µm)
Mesh	5x5	10x10	15x15	20x20	5x5	10x10	15x15	20x20	5x5	10x10	15x15	20x20	
No Aging	9.43	9.17	9.11	9.13	8.24	8.59	8.45	8.55	6.51	6.53	6.41	6.38	8.02
1 M 25 ºC	15,7	14.5	14.1	13.8	10.6	11.1	10.8	11.1	10.1	9.86	9.92	10.2	11.7
1 M 125 ºC	16.7	16.1	16.3	16.4	18.3	17.4	17.3	17.2	17.0	16.7	16.5	16.6	16.7

Table 5.1 Calculation of Mean Lineal Intercept Length L for SACX with No Aging, Aging at 25 ºC, and Aging at 125 ºC
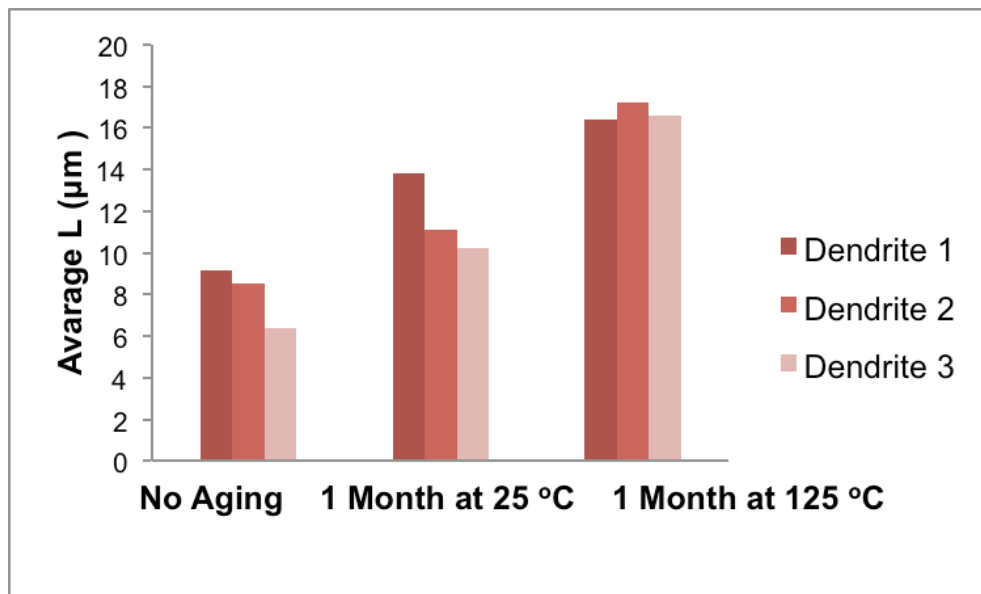
Figure 5.3 Average Intercept Length L of SACX with No Aging, 1 Month Aging at 25 $^{\circ}$C, and 1 Month Aging at 125 $^{\circ}$C

CHAPTER 6

MEASUREMENT OF GRAIN ORIENTATION
OF LEAD FREE SOLDER JOINTS

6.1   Grain Structure Investigation

An OLYMPUS BX60 optical microscope with polarized light was utilized to identify the grain structures and orientations in a bulk SAC105 solder sample. Different colors represent different crystallographic orientations. Figure 6.1 shows the grain structure of the bulk specimen. The polarized optical micrograph illustrates the bulk specimen contains five β-Sn grains, and each grain has a different crystallographic orientation. For each grain, inverse pole figures (IPFs) about three sample axes were generated from EBSD measurements, as shown in Figure 6.2. These measurements determined the orientations of the crystallographic directions with respect to the three sample axes for the grain. The spot with the strongest intensity in each IPF is related to the orientation information for the β-Sn matrix, while the spot with the weaker peak in each IPF corresponds to the orientation information for the Cu_6Sn_5 and Ag_3Sn (IMC) in the solder alloy. Due to the variety of crystallographic orientations and mechanical properties for the different grains, it is expected that tensile testing of such a bulk specimen would yield a set of mechanical property values that represented the average values for the various grains.

An iNEMI solder test board (see Figure 6.3) was used to study solder joints. A cross-section was prepared for the larger 14 x 14 mm PBGA package, which contained
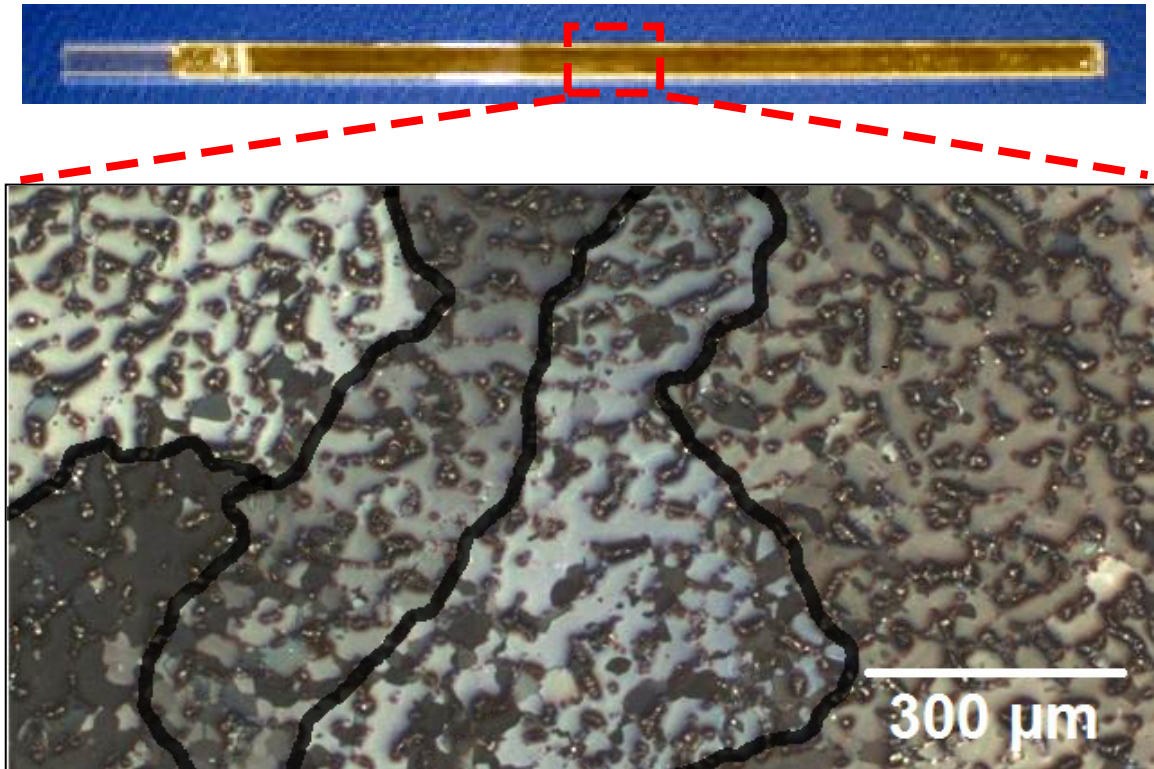
Figure 6.1 Polarized Light Image of Grain Structure in the Bulk SAC105 Solder

Specimen
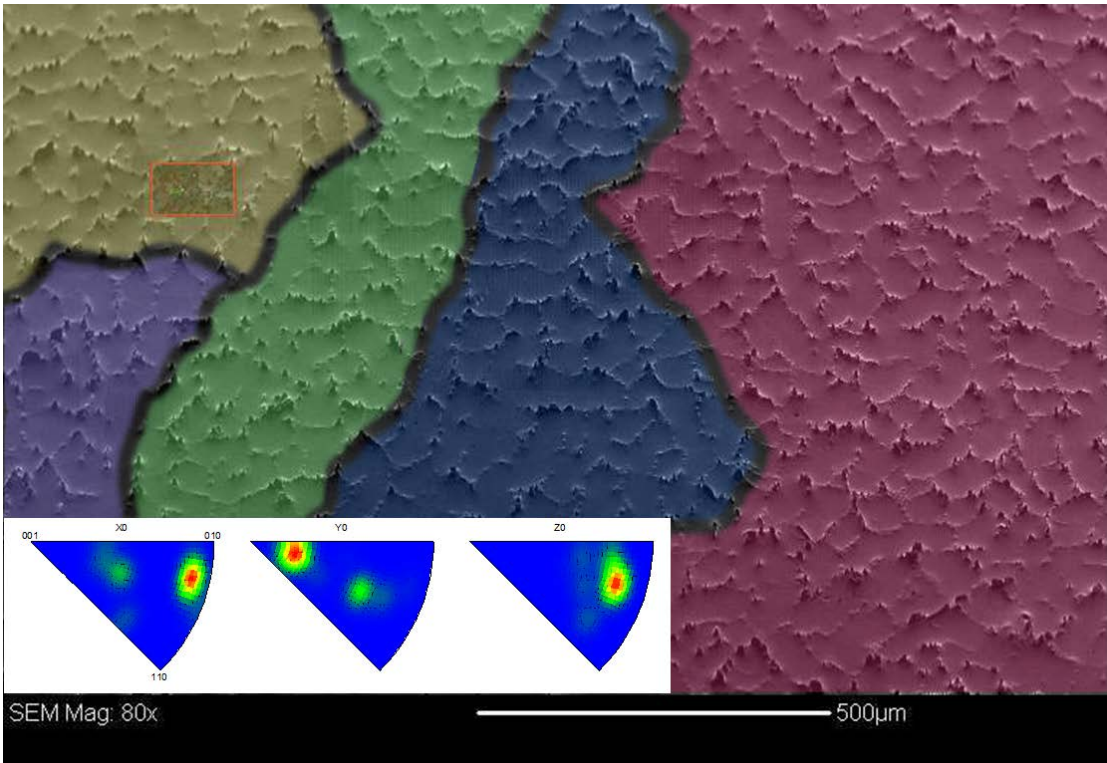
(a) EBSD Scanning Map and IPF for Grain 1
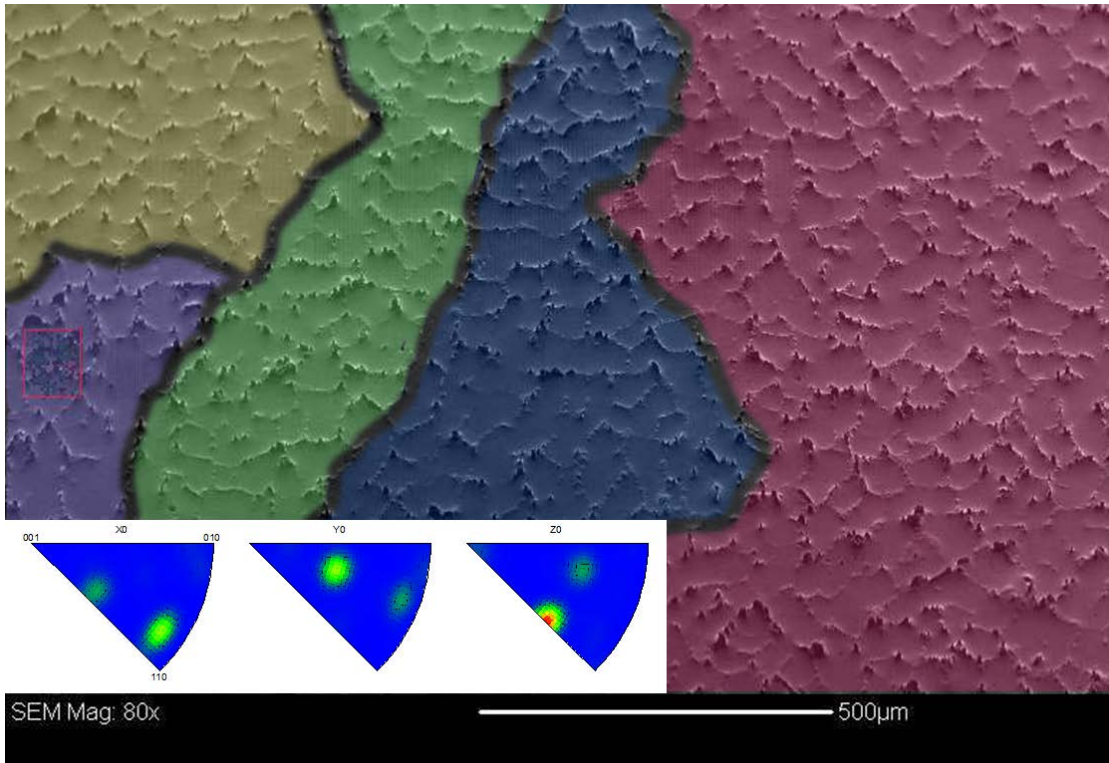
(b) EBSD Scanning Map and IPF for Grain 2
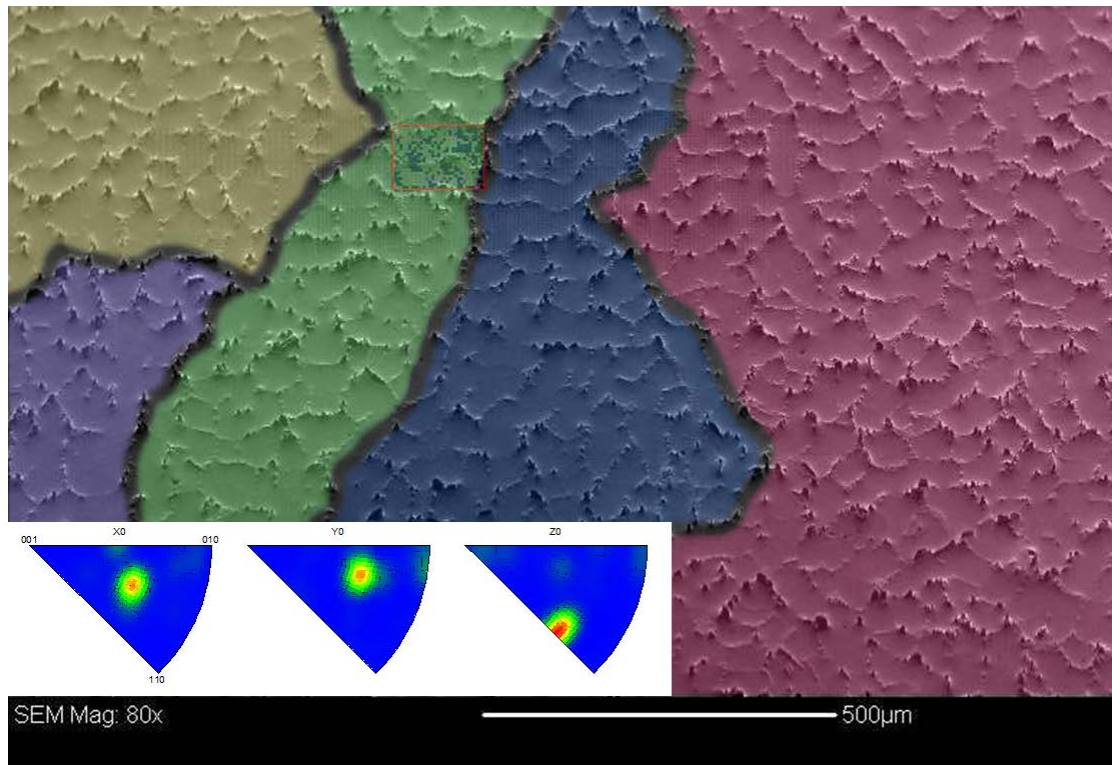
(c) EBSD Scanning Map and IPF for Grain 3
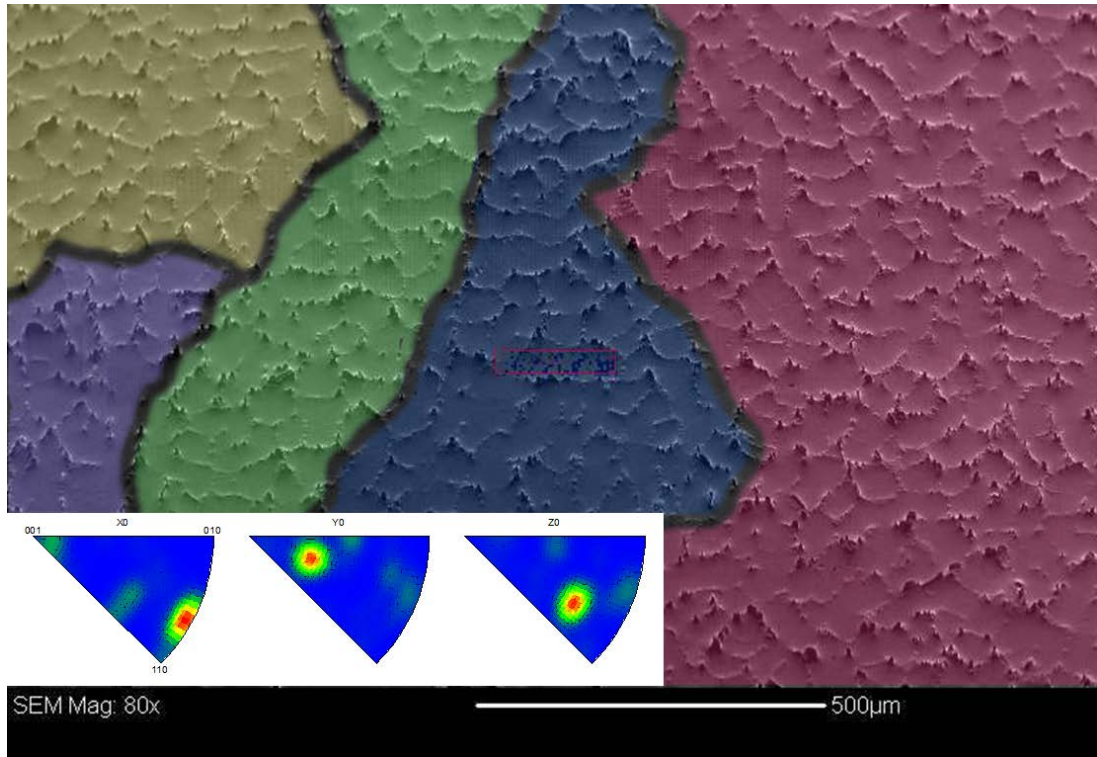
(d) EBSD Scanning Map and IPF for Grain 4
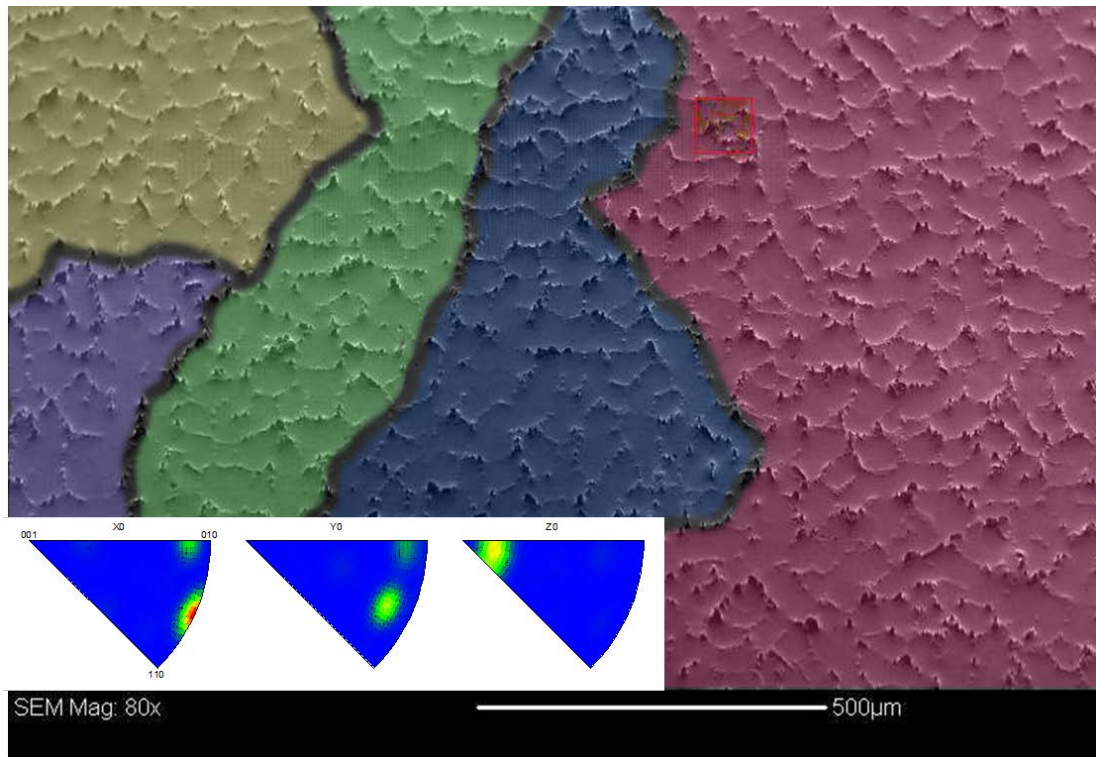
(e) EBSD Scanning Map and IPF for Grain 5

Figure 6.2 EBSD Scanning Maps and IPFs for the Bulk SAC 105 Specimen
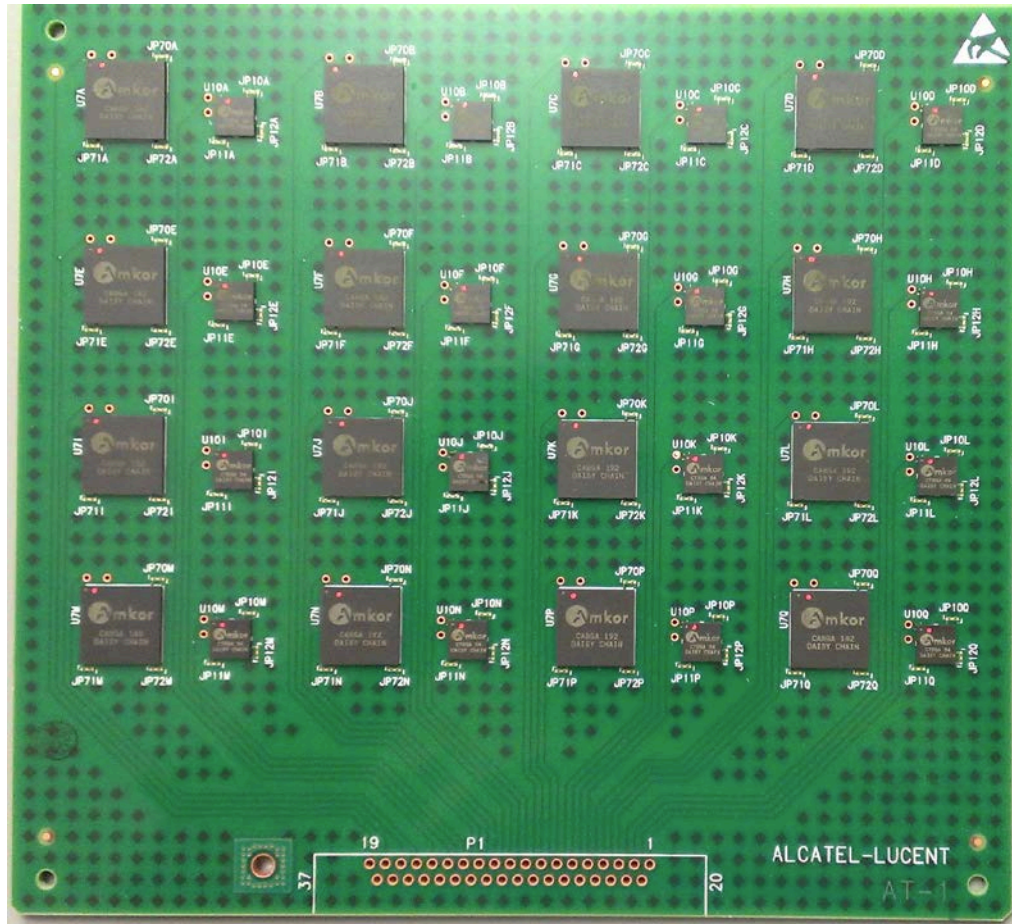
Figure 6.3 iNEMI Solder Test Vehicle

an area array of SAC305 solder balls with a 0.8 mm pitch. For each solder ball, an individual polarized light micrograph was taken. Several images were combined to represent the entire row of joints in the package, as illustrated in Figure 6.4. It was observed that each solder joint contained one or more β-Sn grains, which is similar to the observation of others [38].

6.2 Crystallographic Plane Determination

A particular example of a solder ball with a two-grain structure is shown in Figure 6.5. The scanning map in Figure 6.6 was obtained using the EBSD system and the area in the solder joint was scanned with a 5 μm step size. The results corresponded well with the polarized light image, which provided a more complete and detailed view of the grain structures and orientations. The points not appearing in the mapping were due to regions of high concentrations of Cu_6Sn_5 and Ag_3Sn (IMC). The available phase database of β-Sn only was used for the EBSD scanning.

From the EBSD data, three Euler angles were obtained for each grain, as shown in Table 6.1. Euler angles are widely used to define the orientation of a sample relative to the crystal, which are formed from rotating the sample coordinate system by φ_1 about the z'-axis, ϕ about the x-axis, and φ_1 about the z-axis until the sample coordinate system comes into coincidence with the crystallographic coordinate system, as shown in Figure 6.7. The relationship between the sample coordinates and the crystallographic coordinates is established by the following vector transformation:

$$\begin{bmatrix} x \\ y \\ z \end{bmatrix} = \begin{bmatrix} \cos\varphi_2 & \sin\varphi_2 & 0 \\ -\sin\varphi_2 & \cos\varphi_2 & 0 \\ 0 & 0 & 1 \end{bmatrix} \begin{bmatrix} 1 & 0 & 0 \\ 0 & \cos\phi & \sin\phi \\ 0 & -\sin\phi & \cos\phi \end{bmatrix} \begin{bmatrix} \cos\varphi_1 & \sin\varphi_1 & 0 \\ -\sin\varphi_1 & \cos\varphi_1 & 0 \\ 0 & 0 & 1 \end{bmatrix} \begin{bmatrix} x' \\ y' \\ z' \end{bmatrix} \qquad (6.1)$$
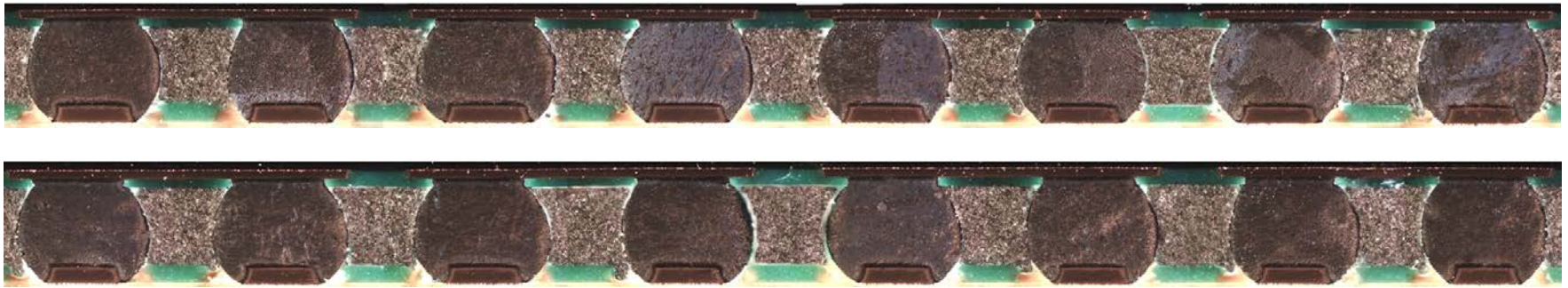
Figure 6.4 Polarized Light Images of a Cross Section of Sixteen SAC 305 Solder Balls
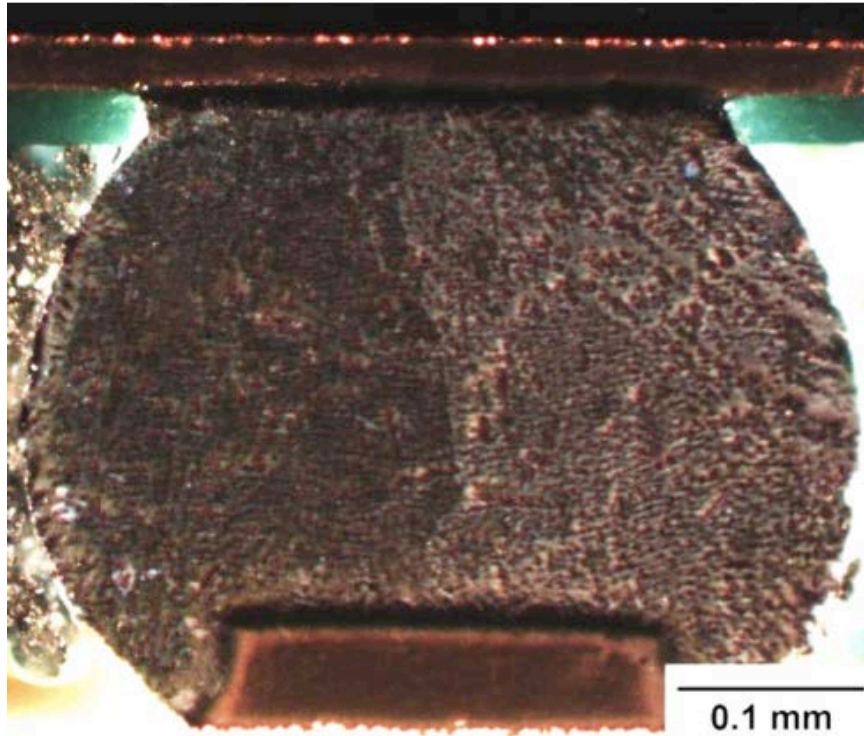
Figure 6.5 Polarized Light images of a SAC 305 Solder Joint
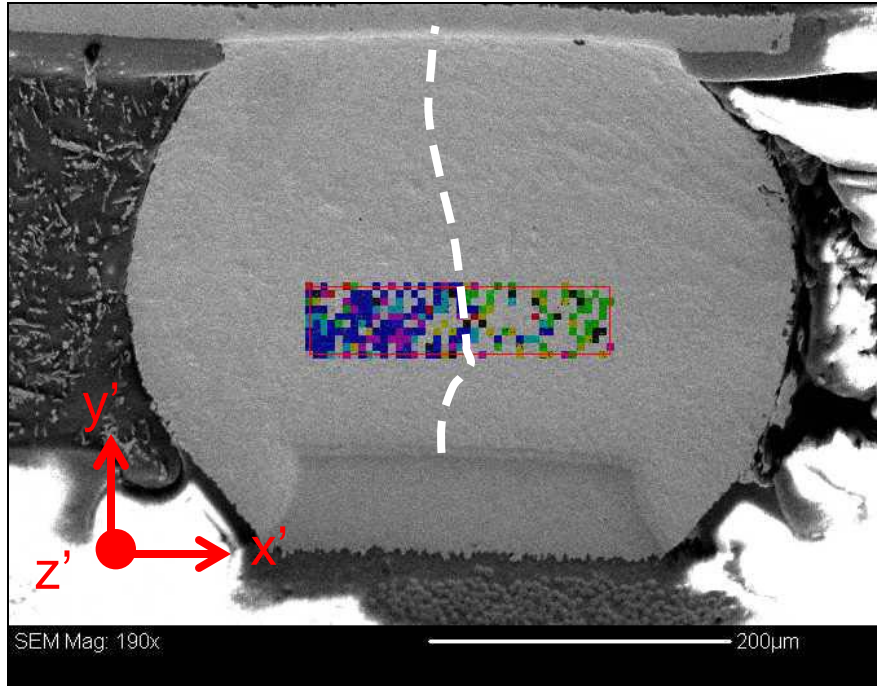
Figure 6.6 EBSD Scanning Map for a SAC 305 Solder Joint

Grain	φ_1 [^{o}]	ϕ [^{o}]	φ_1 [^{o}]
Left	139.23	72.66	15.63
Right	33.17	129.29	43.74

Table 6.1 Euler Angles for the Two Grains in the SAC 305 Solder Joint
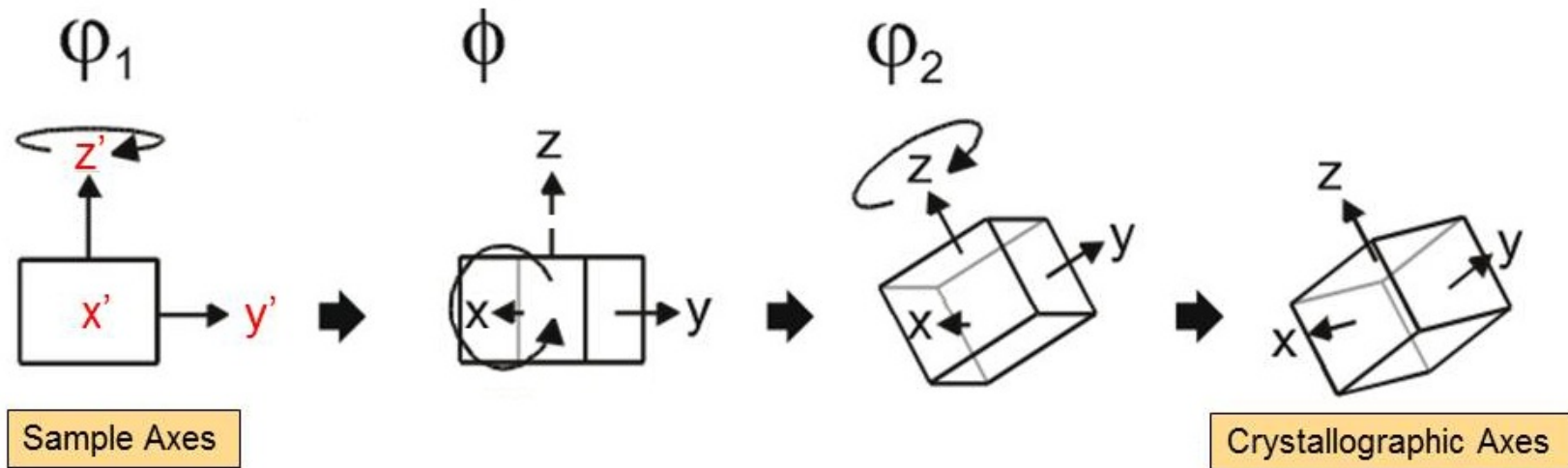
Figure 6.7 Formation of Euler Angles

The crystallographic orientation can be obtained based on the calculation of the vector transformation. For example, the crystallographic plane in the left grain perpendicular to the x' axis has a unit vector [1 0 0] in the sample coordinates. Using the equation of the vector transformation, the unit vector is transformed to be [-0.7818 0.0165 0.6233] in the crystallographic coordinates.

A particular plane can be expressed by the equation☐Ax + By + Cz + D = 0, where A, B, C and D are constants. The vector [A B C] is a normal vector of the plane. For the transformed vector in the crystallographic coordinates [x y z] = [-0.7818 0.0165 0.6233], the plane perpendicular to the unit vector can be written as☐-0.7818x + 0.0165y + 0.6233z + D = 0. Then the intercepts of the x-axis, y-axis, and z-axis are equal to D/-0.7818, D/0.0165, and D/0.6233, respectively. In the unit cell of β-Sn as shown in Figure 6.8, the plane (h k l) has three intercepts, given by a/h (x-intercept), a/k (y-intercept) and c/l (x-intercept), where h, k, l are miller indices of the plane. Therefore, D/-0.7818 = 5.8315/h and h = -4.5590/D; D/0.0165 = 5.8315/k and k = 0.0962/D; D/0.6233 = 3.1814/l and l =1.9830/D. By converting h, k, l to integers, the plane perpendicular to the transformed vector in the crystallographic coordinates was found to be (-7 0 3) for the left grain. Using the same method as discussed, the plane with respect to the y' axis was found to be (3 -2 2) and plane with respect to the z' axis was found to be (3 11 2) for the left grain. The plane orientation of the right grain was also obtained as illustrated in Table 6.2.

6.3   Inverse Pole Figure and Pole Figure

A Matlab program, shown in Appendix III, was developed for generating a (001) stereographic projection of a β-Sn grain. Based on the crystallographic plane calculation,
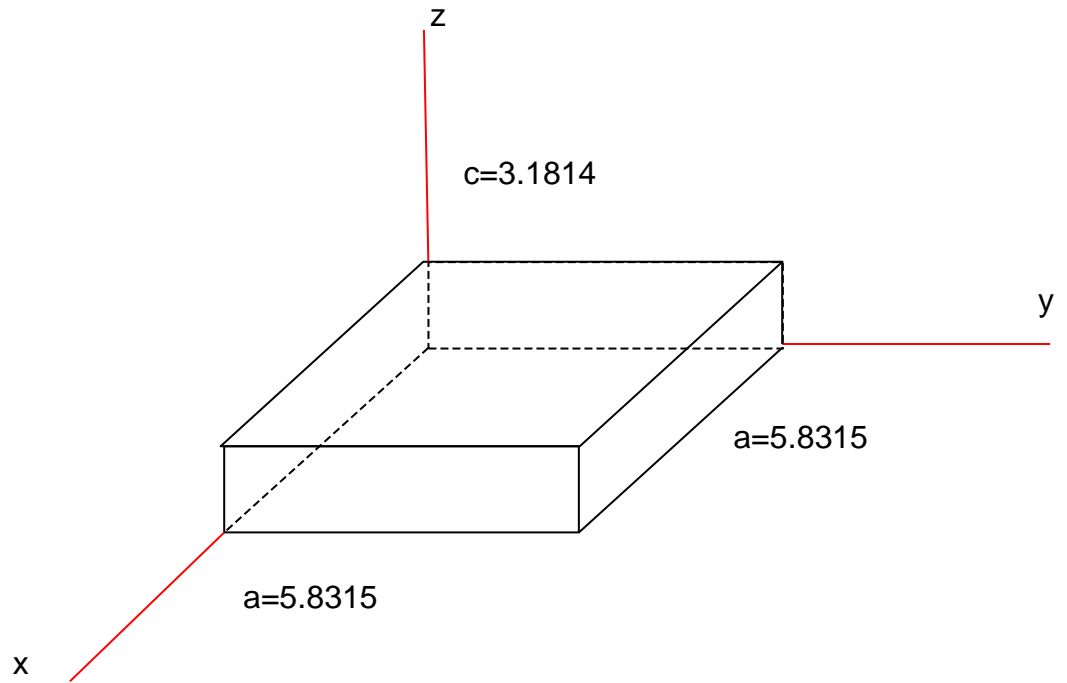
Figure 6.8 β-Sn Unit Cell in Crystallographic Coordinates

Grain	Unit Vector in Sample Coordinate	Unit Vector in Crystallographic Coordinate	Miller Indices			Plane
	[x' y' z']	[x y z]	h	k	l	
Left	[1 0 0]	[-0.7818 0.0165 0.6233]	-4.5590	0.0962	1.9830	(-7 0 3)
	[0 1 0]	[0.5680 -0.3934 0.7229]	3.3123	-2.2941	2.2998	(3 -2 2)
	[0 0 1]	[0.2572 0.9192 0.2982]	1.4999	5.3603	0.9487	(3 11 2)
Right	[1 0 0]	[0.8443 -0.3284 0.4235]	4.9235	-1.9151	1.3473	(7 -3 2)
	[0 1 0]	[0.0289 -0.7612 -0.6478]	0.1685	-4.4389	-2.0609	(0 2 1)
	[0 0 1]	[0.5351 0.5592 -0.6332]	3.1204	3.2610	-2.0145	(-3 -3 2)

Table 6.2 Calculation of Plane Orientations for the Two Grains in the SAC 305 Solder Joint

IPFs about the x', y' and z' axes for the left grain and right grain were generated as shown in Figure 6.9. The results corresponded well with the IPF maps derived from OIM measurements directly, as shown in the middle of Figure 6.9. Color OIM maps of EBSD are also used to illustrate the crystallographic orientation information for each grain. The OIM data sets in the maps are cleaned up by removing Ag_3Sn and Cu_6Sn_5 (IMC) particles and using a nearest neighbor correlation technique (incorporating lower confidence index points to the neighboring index points with higher confidence). This agreement proves the accuracy of the calculation of crystallographic orientations from the Euler angles analysis. Also, the crystallographic orientation of plane {100}, {110} and {111} can be plotted on the pole figures, as shown in Figure 6.10.

6.4   Summary and Discussion

A combination of an optical microscopy with polarized light and the EBSD method was used to characterize the grain structures and orientations of a bulk SAC 105 solder sample and a SAC 305 solder joint. Multi-grain structures were identified by these two measurements. Three Euler angles were obtained from the EBSD data and applied to calculate the crystallographic orientations of the different grains. Based on a Matlab program, the correlation between grain orientations and IPFs of SAC solder joints were generated. IPFs obtained from the Matlab program agreed well with the ones produced from the EBSD data using the post-processing software Mambo.
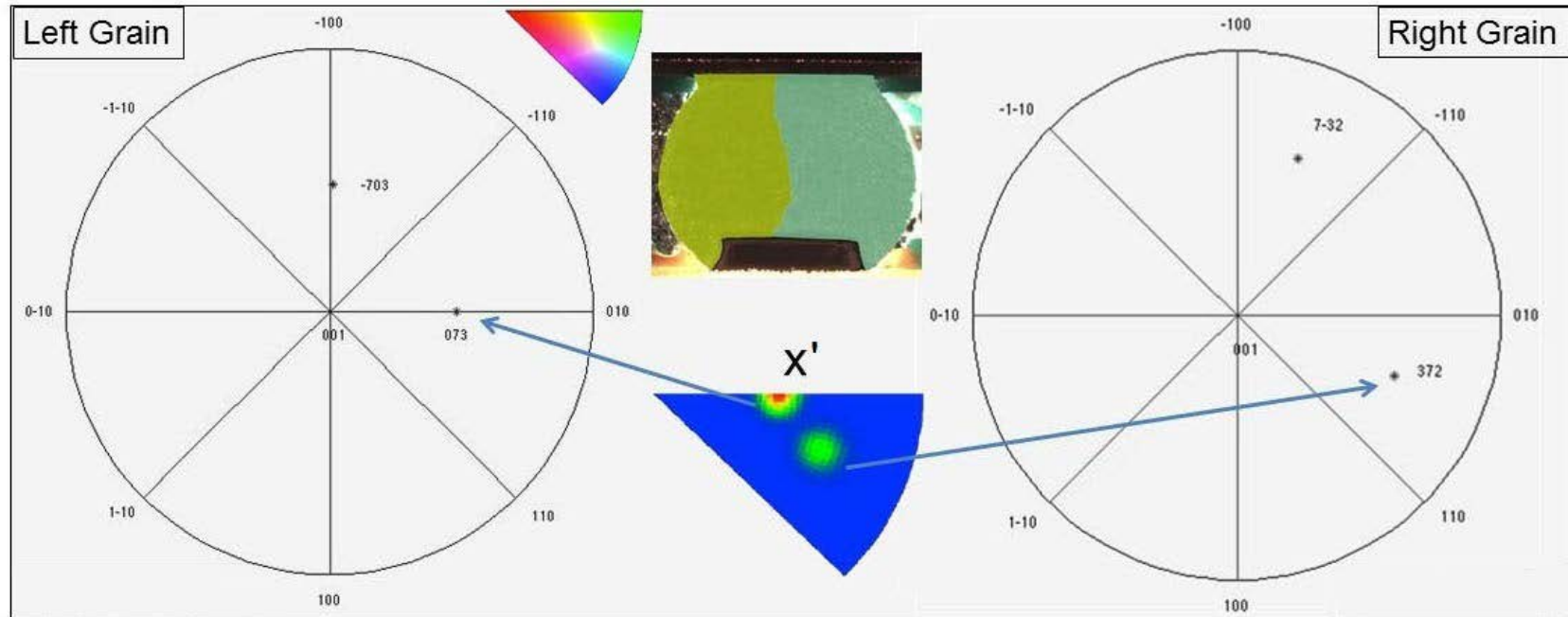
(a) IPF about x' Axis
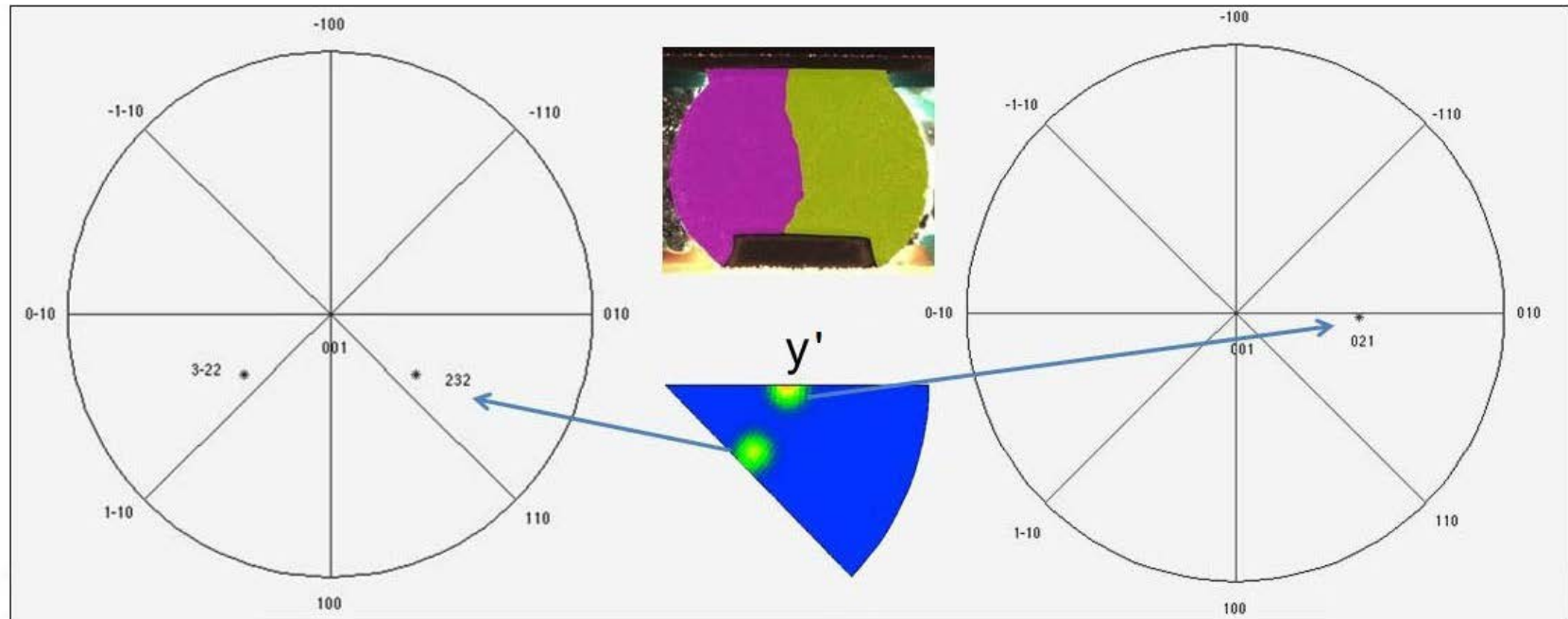
(b) IPF about y' Axis
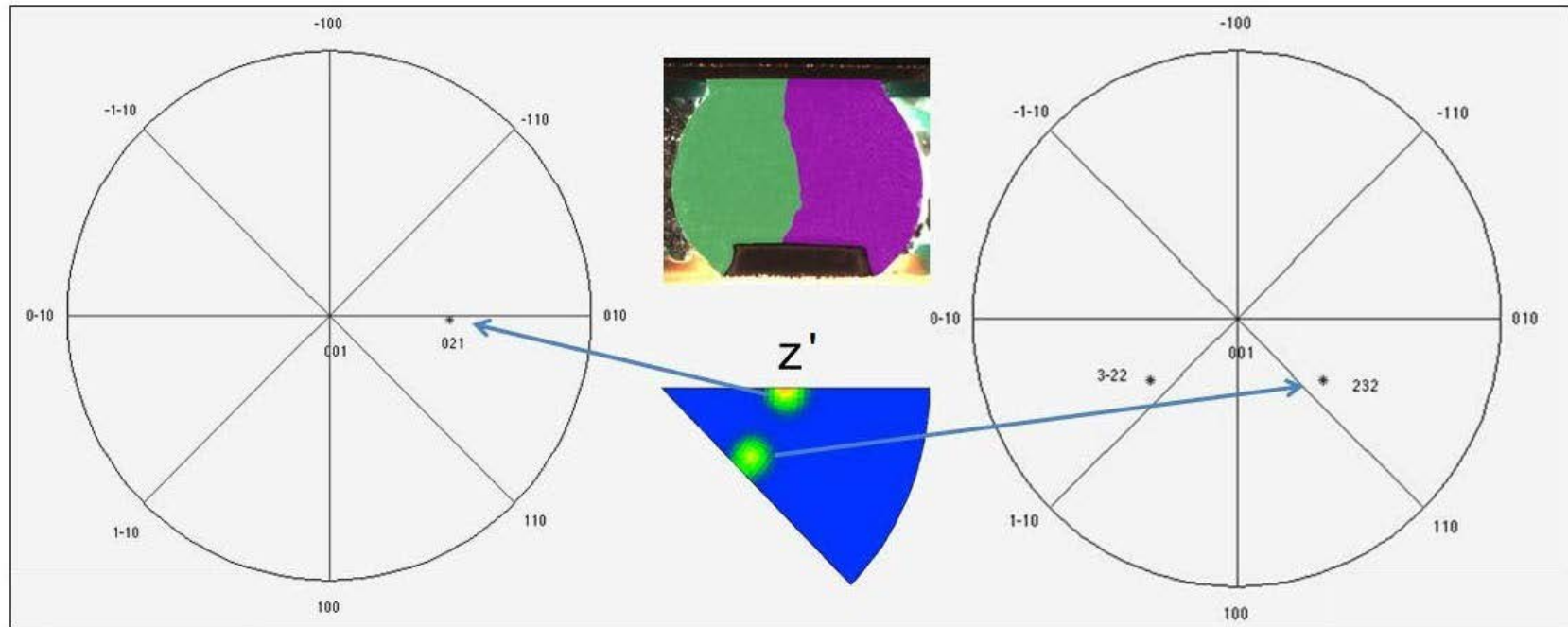
(c) IPF about z' Axis

Figure 6.9 IPF for the Two Grains in the SAC 305 Solder Joint
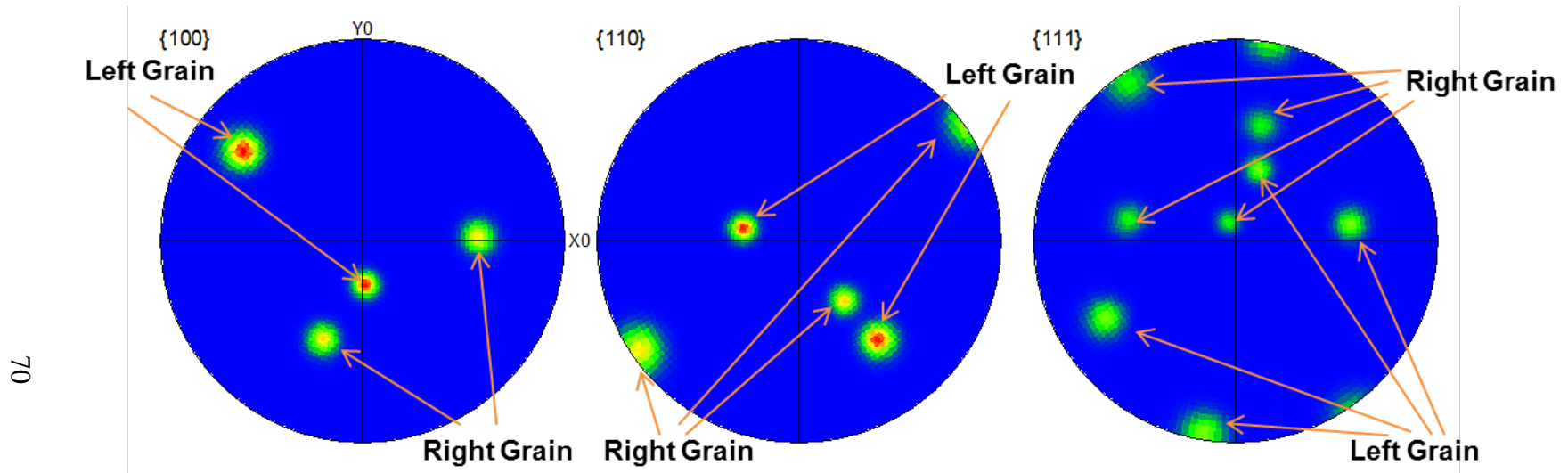
Figure 6.10 Pole Figure for the Two Grains in SAC 305 Solder Joint

CHAPTER 7

EFFECT OF GRAIN ORIENTATION ON MECHANICAL RESPONSE
OF LEAD FREE SOLDER JOINTS

7.1   Effect of Grain Orientation on Elastic Modulus

Due to the anisotropy of β-Sn structure and primary β-Sn matrix in solder joints, the elastic modulus of each grain in a solder joint varies with the orientation of the β-Sn grain. The elastic modulus of β-Sn in an arbitrary direction can be calculated using the following equation [27]:

$$\frac{1}{E_n} = S_{11}\left(\gamma_1^4 + \gamma_2^4\right) + 2S_{12}\gamma_1^2\gamma_2^2 + 2S_{13}\left(\gamma_1^2\gamma_3^2 + \gamma_2^2\gamma_3^2\right) + S_{33}\gamma_3^4 + S_{44}\left(\gamma_1^2\gamma_3^2 + \gamma_2^2\gamma_3^2\right) + S_{66}\gamma_1^2\gamma_2^2 \quad (7.1)$$

where γ_i (i = 1, 2, 3) are the directional cosines of a unit vector in the n-direction with respect to the three crystallographic directions (the x, y, and z axes). The material constants of β-Sn are given by S_{11}=41.6 /TPa, S_{33}=14.9 /TPa, S_{44}=45.6 /TPa, S_{66}=42.8 /TPa, S_{12}=-31.2 /TPa, and S_{13}=-4.8 /TPa, which were measured by vibration experiments for circular cylinder rods of tin single crystals at 15 °C [27].

Table 7.1 shows the calculations of the elastic moduli for the two grains in the solder joint in Figure 6.5. For the plane (-7 0 3) perpendicular to the x' axis of the left grain, γ_1, γ_2, and γ_3 are -0.7818, 0.0165, and 0.6233, respectively, which gives elastic modulus E_n = 38.00 GPa using Equation 7.1. This means the elastic modulus along the x' axis E_x is 38.00 GPa. Also, elastic modulus along the y' axis E_y and elastic modulus

Grain	Unit Vector in Sample Coordinate	Unit Vector in Crystallographic Coordinate	Plane	E_n
	[x' y' z']	[x y z]		
Left	[1 0 0]	[-0.7818 0.0165 0.6233]	(-7 0 3)	38.00
	[0 1 0]	[0.5680 -0.3934 0.7229]	(3 -2 2)	57.48
	[0 0 1]	[0.2572 0.9192 0.2982]	(3 11 2)	31.43
Right	[1 0 0]	[0.8443 -0.3284 0.4235]	(7 -3 2)	38.62
	[0 1 0]	[0.0289 -0.7612 -0.6478]	(0 2 1)	39.45
	[0 0 1]	[0.5351 0.5592 -0.6332]	(-3 -3 2)	59.65

Table 7.1 Calculation of E_n for the Two Grains in SAC 305 Solder Joint

along the z' axis E_z for the left grain can be calculated as 57.48 GPa and 31.43 GPa, respectively.

A unit vector transformation between the sample coordinate system and the crystallographic coordinate system can be described as:

$$\begin{bmatrix} x \\ y \\ z \end{bmatrix} = \begin{bmatrix} a_{11} & a_{12} & a_{13} \\ a_{21} & a_{22} & a_{23} \\ a_{31} & a_{32} & a_{33} \end{bmatrix} \begin{bmatrix} x' \\ y' \\ z' \end{bmatrix} \tag{7.2}$$

where

$$a_{11} = \cos(x, x') = \cos\phi_1 \cos\phi_2 - \cos\varphi \sin\phi_1 \sin\phi_2$$
$$a_{12} = \cos(x, y') = \cos\phi_2 \sin\phi_1 + \cos\phi_1 \cos\varphi \sin\phi_2$$
$$a_{13} = \cos(x, z') = \sin\varphi \sin\phi_2$$
$$a_{21} = \cos(y, x') = -\cos\phi_1 \cos\phi_2 - \cos\varphi \sin\phi_2 \sin\phi_1$$
$$a_{22} = \cos(y, y') = \cos\phi_1 \cos\varphi \cos\phi_2 - \sin\phi_1 \sin\phi_2$$
$$a_{23} = \cos(y, z') = \cos\phi_2 \sin\varphi$$
$$a_{31} = \cos(z, x') = \sin\phi_1 \sin\varphi$$
$$a_{32} = \cos(z, y') = -\cos\phi_1 \sin\varphi$$
$$a_{33} = \cos(z, z') = \cos\varphi$$

(φ_1, ϕ, φ_2 are the Euler angles)

For an arbitrary n-direction,

$$x = \gamma_1; y = \gamma_2; z = \gamma_3; x' = \gamma_1'; y' = \gamma_2'; z' = \gamma_3' \tag{7.3}$$

Based on Equation 7.2 and 7.3, the direction cosines of the n-direction transformation can be formulated as the following equation:

$$\gamma_1 = x = a_{11}x' + a_{12}y' + a_{13}z' = a_{11}\gamma_1' + a_{12}\gamma_2' + a_{13}\gamma_3'$$
$$\gamma_2 = y = a_{21}x' + a_{22}y' + a_{23}z' = a_{21}\gamma_1' + a_{22}\gamma_2' + a_{23}\gamma_3' \tag{7.4}$$
$$\gamma_3 = z = a_{31}x' + a_{32}y' + a_{33}z' = a_{31}\gamma_1' + a_{32}\gamma_2' + a_{33}\gamma_3'$$

Substituting Equation 7.4 and a_{ij} (where i and j take values ranging from 1 to 3) into Equation 7.1, the theoretical elastic modulus in an arbitrary direction of the sample coordinate system can be obtained:

$$
\begin{aligned}
\frac{1}{E_n} =& S_{11}\left\{\begin{array}{l}\left[(\cos\phi_1\cos\phi_2-\cos\varphi\sin\phi_1\sin\phi_2)\gamma_1'+(\cos\phi_2\sin\phi_1+\cos\phi_1\cos\varphi\sin\phi_2)\gamma_2'+(\sin\varphi\sin\phi_2)\gamma_3'\right]^4 \\ +\left[(-\cos\phi_1\sin\phi_2-\cos\varphi\cos\phi_2\sin\phi_1)\gamma_1'+(\cos\phi_1\cos\varphi\cos\phi_2-\sin\phi_1\sin\phi_2)\gamma_2'+(\cos\phi_2\sin\varphi)\gamma_3'\right]^4\end{array}\right\} \\
&+2S_{12}\left\{\begin{array}{l}\left[(\cos\phi_1\cos\phi_2-\cos\varphi\sin\phi_1\sin\phi_2)\gamma_1'+(\cos\phi_2\sin\phi_1+\cos\phi_1\cos\varphi\sin\phi_2)\gamma_2'+(\sin\varphi\sin\phi_2)\gamma_3'\right]^2 \\ \left[(-\cos\phi_1\sin\phi_2-\cos\varphi\cos\phi_2\sin\phi_1)\gamma_1'+(\cos\phi_1\cos\varphi\cos\phi_2-\sin\phi_1\sin\phi_2)\gamma_2'+(\cos\phi_2\sin\varphi)\gamma_3'\right]^2\end{array}\right\} \\
&+2S_{13}\left\{\begin{array}{l}\left[(\cos\phi_1\cos\phi_2-\cos\varphi\sin\phi_1\sin\phi_2)\gamma_1'+(\cos\phi_2\sin\phi_1+\cos\phi_1\cos\varphi\sin\phi_2)\gamma_2'+(\sin\varphi\sin\phi_2)\gamma_3'\right]^2 \\ \left[(\sin\phi_1\sin\varphi)\gamma_1'+(-\cos\phi_1\sin\varphi)\gamma_2'+(\cos\varphi)\gamma_3'\right]^2 \\ +\left[(-\cos\phi_1\sin\phi_2-\cos\varphi\cos\phi_2\sin\phi_1)\gamma_1'+(\cos\phi_1\cos\varphi\cos\phi_2-\sin\phi_1\sin\phi_2)\gamma_2'+(\cos\phi_2\sin\varphi)\gamma_3'\right]^2 \\ \left[(\sin\phi_1\sin\varphi)\gamma_1'+(-\cos\phi_1\sin\varphi)\gamma_2'+(\cos\varphi)\gamma_3'\right]^2\end{array}\right\} \\
&+S_{33}\left[(\sin\phi_1\sin\varphi)\gamma_1'+(-\cos\phi_1\sin\varphi)\gamma_2'+(\cos\varphi)\gamma_3'\right]^4 \\
&+S_{44}\left\{\begin{array}{l}\left[(\cos\phi_1\cos\phi_2-\cos\varphi\sin\phi_1\sin\phi_2)\gamma_1'+(\cos\phi_2\sin\phi_1+\cos\phi_1\cos\varphi\sin\phi_2)\gamma_2'+(\sin\varphi\sin\phi_2)\gamma_3'\right]^2 \\ \left[(\sin\phi_1\sin\varphi)\gamma_1'+(-\cos\phi_1\sin\varphi)\gamma_2'+(\cos\varphi)\gamma_3'\right]^2 \\ +\left[(-\cos\phi_1\sin\phi_2-\cos\varphi\cos\phi_2\sin\phi_1)\gamma_1'+(\cos\phi_1\cos\varphi\cos\phi_2-\sin\phi_1\sin\phi_2)\gamma_2'+(\cos\phi_2\sin\varphi)\gamma_3'\right]^2 \\ \left[(\sin\phi_1\sin\varphi)\gamma_1'+(-\cos\phi_1\sin\varphi)\gamma_2'+(\cos\varphi)\gamma_3'\right]^2\end{array}\right\} \\
&+S_{66}\left\{\begin{array}{l}\left[(\cos\phi_1\cos\phi_2-\cos\varphi\sin\phi_1\sin\phi_2)\gamma_1'+(\cos\phi_2\sin\phi_1+\cos\phi_1\cos\varphi\sin\phi_2)\gamma_2'+(\sin\varphi\sin\phi_2)\gamma_3'\right]^2 \\ \left[(-\cos\phi_1\sin\phi_2-\cos\varphi\cos\phi_2\sin\phi_1)\gamma_1'+(\cos\phi_1\cos\varphi\cos\phi_2-\sin\phi_1\sin\phi_2)\gamma_2'+(\cos\phi_2\sin\varphi)\gamma_3'\right]^2\end{array}\right\}
\end{aligned}
\tag{7.5}
$$

where S_{11}=42.4 /TPa, S_{33}=14.8 /TPa, S_{44}=45.6 /TPa, S_{66}=42.1 /TPa, S_{12}=-32.4 /TPa, S_{13}=-4.3 /TPa and γ_i' (i = 1, 2, 3) are the directional cosines of a unit vector in the n-direction with respect to the three sample coordinate directions (the x', y', and z' axes).

7.2   Finite Element Analysis (FEA) Modeling

Conventional finite element method (FEM) models have not taken into account the anisotropy of β-Sn grains in the solder joints. In this study, simple planar finite element models were generated to predict mechanical behaviors of solder joints corresponding to different grain structures and orientations. Three simple finite element

models of the assembly are shown in Figure 7.1. They were built with anisotropic material properties of the solder (elastic moduli of grains 1 and 2) obtained from the previous calculations, and isotropic material properties of package materials (PCB, BT substrate and copper) available in the literature [39], as listed in Table 7.2. The left and right finite element models used the Grain 1 and Grain 2 materials, respectively. For the middle finite element model, the material in the left part of the solder was Grain 1, and the material in the right part of the solder was Grain 2. A pure shear mechanical loading was applied to simulate a thermal cycling experiment that will induce mechanical loads due to mismatches in coefficients of thermal expansion (CTEs) of package materials.

In the contour plot, the in-plane shear stress concentrations are most likely along the grain boundaries for two β-Sn grain structures of the middle model. The observation can be explained by the mismatch of elastic moduli for the two grains. This phenomenon agrees well with others' observation [40]. It has been reported that the anisotropy of β-Sn elastic modulus and thermal expansion coefficients lead to shear strains along grain boundaries under the thermal loading.

Also the results show that the maximum in-plane shear stress (σ_{xy}) for the left model is 47.7 MPa, which occurs at the interface of solder joint and the copper pad while the maximum in-plane shear stresses (σ_{xy}) for the middle and right models are 44.7 MPa and 43.5 MPa, respectively, which occur at the interface of copper pad and BT substrate. It has been reported that cracks initiated and propagated predominantly along the interface of the copper pad with the solder joint [41]. That means cracks will very likely form early in the solder joint of the left model compared to the solder joints of the middle or right model.

Materials Name	Elastic Modulus (GPa)		Poisson's Ratio
Grain 1	37.23 (X)	56.92 (Y)	0.35
Grain 2	38.14 (X)	38.70 (Y)	0.35
PCB	27.924		0.11
BT	17.89		0.11
Cooper	129		0.34

Table 7.2 Mechanical Properties of Package Materials [39]
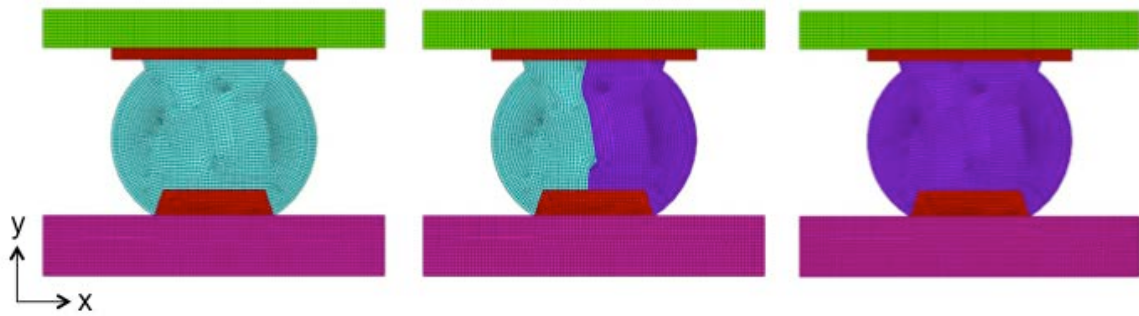
Figure 7.1 FEA Modeling for Solder Joints with Different Grain Structures
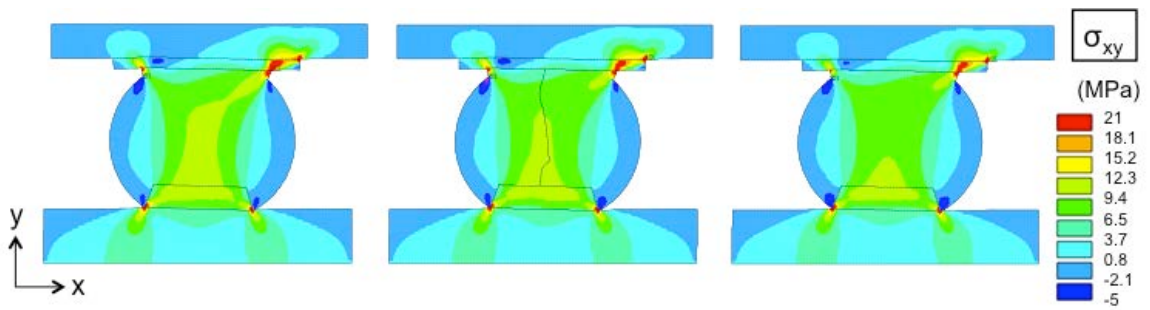
Figure 7.2 FEA Results for In-Plane Shear Stress

7.3   Summary and Discussion

Since SAC solder joints cannot be treated as homogeneous and isotropic materials, the elastic modulus of SAC solder joints is directionally dependent, varying with grain orientation. Some equations have been developed for the calculation of elastic modulus based on the orientation of β-Sn grain. To simulate the thermal cycling experiment for solder joints in the electronic package, simple finite element models were built for a typical solder joint by considering grain structures and grain orientations. By analyzing the distributions of in-plane shear stress, concentrations were induced along the grain boundary due to the mismatch of different grain properties. Also the location of the maximum in-plane shear stress changed for different grain structures and orientations, which would affect the failure behaviors of solder joints.

CHAPTER 8

CONCLUSIONS

Lead free solders, especially SAC solders, have been widely used in electronic packaging to replace leaded solder alloys. SAC solder alloys have β-Sn matrices with more than 95 wt.% and a small amount of precipitation of Cu_6Sn_5 and Ag_3Sn IMC. Due to the anisotropic nature of the tetragonal lattice structure of β-Sn, SAC solders cannot be treated as homogeneous and isotropic materials, and the mechanical responses of SAC solders are direction-sensitive. Thus, the grain structure including grain sizes and grain orientations becomes an important factor in analyzing the mechanical behaviors of SAC solders. An OLYMPUS BX60 optical microscope with polarization filters and an EBSD system (HKL, channel 5) attached to a JEOL JSM-7000F SEM JEOL JSM-7000F SEM were used to examine the microstructures of grains of SAC solders.

Sub-grain sizes were quantitatively measured using three methods: ASTM standard E112-96 based intercept method, planimetric method and EBSD method. For the manual measurements, like the intercept method and planimetric method, the results of the average sub-grain size converged for finer meshing. The results from the planimetric method and EBSD method matched well. The mechanical behaviors can be estimated and predicted based on the measurements of sub-grain sizes. Mechanical properties of SAC solders degrade when grain sizes increase and the numbers of grain decrease. Also the sub-grain sizes are correlated to aging, increasing with aging time.

Thus, aging time induces grain growth, which might result in a reduction in mechanical properties of SAC solders. Also, aging temperature accelerates the aging effect.

Grain orientations were determined by the EBSD measurements and post analysis. Crystallographic orientations were calculated by using three Euler angles. By comparing the IPFs generated from the calculation of Euler angles with those generated from the EBSD data using the post-processing software Mambo, the results of crystallographic orientation corresponded well. According to the plane orientation, the elastic moduli for different grains were calculated by a theoretical equation. Then, the anisotropic mechanical properties were included in a simple finite element model. The in-plane shear stress concentrated along the grain boundaries of two grains with different orientations when applying a pure shear load to simulate the thermal cycling. Also, the maximum in-plane shear stress occurred in different locations of the package, which influenced the failure behaviors. In general, grain sizes and grain orientations have a strong effect on the mechanical responses, which cannot be ignored for the analysis of mechanical properties of SAC solders.

REFERENCE

[1]   Abtew, M., Selvadury, G., "Lead-free Solders in Microelectronics," <u>Material Science and Engineering Reports</u>, Vol. 27, pp. 95-141, 2000.

[2]   Tu, K. N., Zeng, K., "Tin-lead (SnPb) Solder Reaction in Flip Chip Technology," <u>Materials Science and Engineering Reports</u>, Vol. 34 pp. 1-58, 2001.

[3]   Kang, S. K., Sarkhel, A. K., "Lead (Pb)-Free Solders for Electronic Package," <u>Journal of Electronic Materials</u>, Vol. 23(8), pp. 701-707, 1994.

[4]   Suganuma, K., "Advances in Lead-free Electronics Soldering," <u>Current Opinion in Solid State and Materials Science</u>, Vol. 5, pp. 55-64, 2001.

[5]   Ganesan, S., Pecht, M., <u>Lead-free Electronics</u>, Wiley-Interscience Publication, pp. 45-46, 2006.

[6]   Amagai, M., Watanabe, M., Omiya, M., Kishimoto, K., Shibuya, T., "Mechanical Characterization of Sn-Ag-based Lead-free Solders," <u>Microelectronics Reliability</u>, Vol. 42, pp. 951-966, 2002.

[7]   Zeng, K., Tu, K. N., "Six Cases of Reliability Study of Pb-free Solder Joints in Electronic Packaging Technology," <u>Materials Science and Engineering Reports</u>, Vol. 38, pp. 55-105, 2002.

[8]   http://www.ipc.org/3.0_Industry/3.1_Industry_Data/2012/solderQ1-2012.pdf

[9]   Lee, N. C., "Getting Ready for Lead Free Solders," <u>Indium Corporate America</u>, Utica, NY, USA.

[10]   Trumble, B., "Get the Lead Out," <u>IEEE Spectrum</u>, pp. 55-60, 1998.

[11]   Ma, H. T., Suhling, J. C., "A Review of Mechanical Properties of Lead-free Solders for Electronic Packaging," <u>Journal of Materials Science</u>, Vol. 44(5), pp. 1141-1158, 2009.

[12]   Lehman, L.P., Xing, Y., Bieler, T.R., Cotts, E. J., "Cyclic Twin Nucleation in Tin-based Solder Alloys," <u>Acta Materialia</u>, Vol. 58(10), pp. 3546-3556, 2010.

[13]   Wyckoff, R. W. R, <u>Crystal Structure</u>, Interscience Publishers, pp 28-29, 1963.

[14]   Erinc, M., Schreurs, P. J. G., Geers, M. G. D., "Intergranular Thermal Fatigue Damage Evolution in SnAgCu Lead-free Solder," <u>Mechanics of Materials</u>, Vol. 40, pp. 780-791, 2008.

[15]   Ubachs, R. L. J. M., Schreurs, P. J. G., Geers, M. G. D., "Elasto-viscoplastic Nonlocal Damage Modeling of Thermal Fatigue in Anisotropic Lead-free Solder," <u>Mechanics of Materials</u>, Vol. 39, pp. 685-701, 2007.

[16]   Park, S., Dhakal, R., Lehman, L., Cotts, E., "Measurement of Deformations in SnAgCu Solder Interconnects under In Situ Thermal Loading," <u>Acta Materialia</u>, Vol. 55, pp. 3253-3260, 2007.

[17]   Subramanian, K. N., Lee, J., G., "Effect of Anisotropy of Tin on Thermomechanical Behavior of Solder Joints," <u>Journal of Materials Science: Materials in Electronics</u>, Vol. 15, pp. 235-240, 2004.

[18]   Lee, T. K., Zhou, B., Blair, L., Liu, K. C., Bieler, T. R., "Sn-Ag-Cu Solder Joint Microstructure and Orientation Evolution as a Function of Position and Thermal Cycles in Ball Grid Arrays Using Orientation Imaging Microscopy," <u>Journal of Electronic Materials</u>, Vol. 39(12), pp. 2588-2597, 2010.

[19]   Lee, T. K., Zhou, B., Bieler, T. R., "Impact of Isothermal Aging and Sn Grain Orientation on the Long-Term Reliability of Wafer-Level Chip-Scale Package Sn–Ag–Cu Solder Interconnects," <u>IEEE Transactions on Components, Packaging and Manufacturing Technology</u>, Vol. 2(3), pp. 496-501, 2010.

[20]   Krause, M., Muller, M., Petzold, M., Wiese, S., Wolter, K. J., "Scaling Effects on Grain Size and Texture of Lead Free Interconnects Investigations by Electron Backscatter Diffraction and Nanoindentation", <u>Proceedings of the Electronic Components and Technology Conference</u>, pp. 75-81, 2008.

[21]   Erinc, M., Schreurs, P. J. G., Geers, M. G. D., "Intergranular thermal fatigue damage evolution in SnAgCu lead-free solder," <u>Mechanics of Materials</u>, Vol. 40, pp. 780-791, 2008.

[22]   Zhang, Y. F., Cai, Z. J., Mustafa, M., Suhling, J. C., Lall, P., Bozack, M. J., "The Influence of Aging on the Stress-Strain and Creep Behavior of SAC Solder Alloys," <u>Proceedings of ITHERM Conference</u>, 2010.

[23]   Arfaei, B., Xing, Y., Wood, J., Wolcott, J., Tumne, P., Borgesen, P., Cotts, E., "The Effect of Sn Grain Number and Orientation on the Shear Fatigue Life of

SnAgCu Solder Joints," <u>Proceedings of the Electronic Components and Technology Conference</u>, pp. 459-465, 2008.

[24] Xiao, Q., Bailey, H. J, Armstrong, W. D., "Aging Effects on Microstructure and Tensile Property of Sn3.9Ag0.6Cu Solder Alloy," <u>Journal of Electronic Packaging</u>, Vol. 126(2), pp. 208-212, 2004.

[25] Ma, H. T., Suhling, J. C., Lall P., Bozack, M. J., "Reliability of the Aging Lead-free Solder Joint," <u>Proceedings of the 56th Electronic Components and Technology Conference</u>, pp. 849-864, 2006.

[26] Cai, Z. J., Suhling, J. C., Lall P., Bozack, M. J., "Mitigation of Lead Free Solder Aging Effects using Doped SAC-X Alloys," <u>Proceedings of 13th IEEE ITHERM Conference</u>, pp. 896-910, 2012.

[27] House, D. G., Vernon, E. V., "Determination of the Elastic Moduli of Tin Single Crystals, and Their Variation with Temperature," <u>British Journal of Applied Physics</u>, Vol. 11, pp. 254-259, 1960.

[28] Lee, B. Z., Lee, D. N., "Spontaneous Growth Mechanism of Tin Whiskers," <u>Acta Materialia</u>, Vol. 49, pp. 3701-3714, 1998.

[29] Zamiri, A., Bieler, T. R., Pourboghrat, F., "Anisotropic Crystal Plasticity Finite Element Modeling of the Effect of Crystal Orientation and Solder Joint Geometry on Deformation after Temperature Change," <u>Journal of Electronic Materials</u>, Vol. 38(2), pp. 231-240, 2007.

[30] Song, J. M., Huang, B. R., Liu, C. Y., Lai, Y. S., Chiu, Y. T., Huang, T. W., "Nanomechanical Responses of Intermetallic Phase at the Solder Joint Interface - Crystal Orientation and Metallurgical Effects," <u>Materials Science and Engineering A</u>, Vol. 534, pp. 53-59, 2012.

[31] Chateigner, D., Camana, G., Trimby, P., "Textural Analysis of a Microcrystalline Quartz using X-Ray and Electron Backscatter Diffraction (EBSD) Techniques," <u>Materials Science Forum</u>, Vol 408-412, pp. 1675-1680, 2002.

[32] Bieler, T. R., Jiang, H., Lehman, L. P., Kirkpatrick, T., Cotts, E. J., Nandagopal, B., "Influence of Sn Grain Size and Orientation on the Thermomechanical Response and Reliability of Pb-free Solder Joints," <u>IEEE Transactions on Components, and Packaging Technologies</u>, Vol. 31(2), pp. 370-381, 2008.

[33] Villain, J., Mueller, W., Saeed, U., Weipeert, C., Ulrike, C., Artur, S., "Mechanical Behaviour of SAC-Lead Free Solder Alloys with Regard to the Size

Effect and the Crystal Orientation," <u>European Microelectronics and Packaging Conference</u>, 2009.

[34]   ASTM, "Standard E112-96E2," <u>Annual book of ASTM standards</u>, 1996.

[35]   Cullity, B. D., <u>Element of X-Ray Diffraction, 2nd Ed.</u>, Addison-Wesley Publishing Company, pp. 84-85, 1978.

[36]   Allen, S. L., Notis, M. R., Chromik, R. R., Vinci, R. P., "Microstructural Evolution in Lead-Free Solder Alloys: Part I Cast Sn–Ag–Cu Eutectic," <u>Journal of Material Research</u>, Vol. 19(5), 2004.

[37]   Cai, Z. J., Zhang, Y. F., Suhling, J. C., Lall, P., Johnson, R. W, Bozack, M. J., "Reduction of Lead Free Solder Aging Effects Using Doped SAC Alloys," <u>Proceedings of the 60th Electronic Components and Technology Conference</u>, pp. 1493-1511, 2010.

[38]   Zhou, B., Bieler, T. R., Lee, T. R., Liu, K. C., "Crack Development in a Low-Stress PBGA Packagedue to Continuous Recrystallization Leading to Formation of Orientations with [001] Parallel to the Interface," <u>Journal of Electronic Materials</u>, Vol. 39(12), pp. 2669-2679, 2012.

[39]   Lall, P., Islam, M. N., Singh, N., Suhling, J. C., Darveaux, R., "Model for BGA and CSP Reliability in Automotive Underhood Applications," <u>IEEE Transactions on Components, and Packaging Technologies</u>, Vol. 27(3), pp. 585-593, 2004.

[40]   Liu, X. W., Plumbridge, W. J., "Damage Produced in Solder Alloys during Thermal Cycling," <u>Journal of Electronic Materials</u>, Vol. 36(9), pp. 1111-1120, 2007.

[41]   Lall, P., Hinshaw, R., Pandher, R., "Thermo-mechanical Reliability of SAC Leadfree Alloys," <u>Proceedings of ITHERM Conference</u>, 2010.
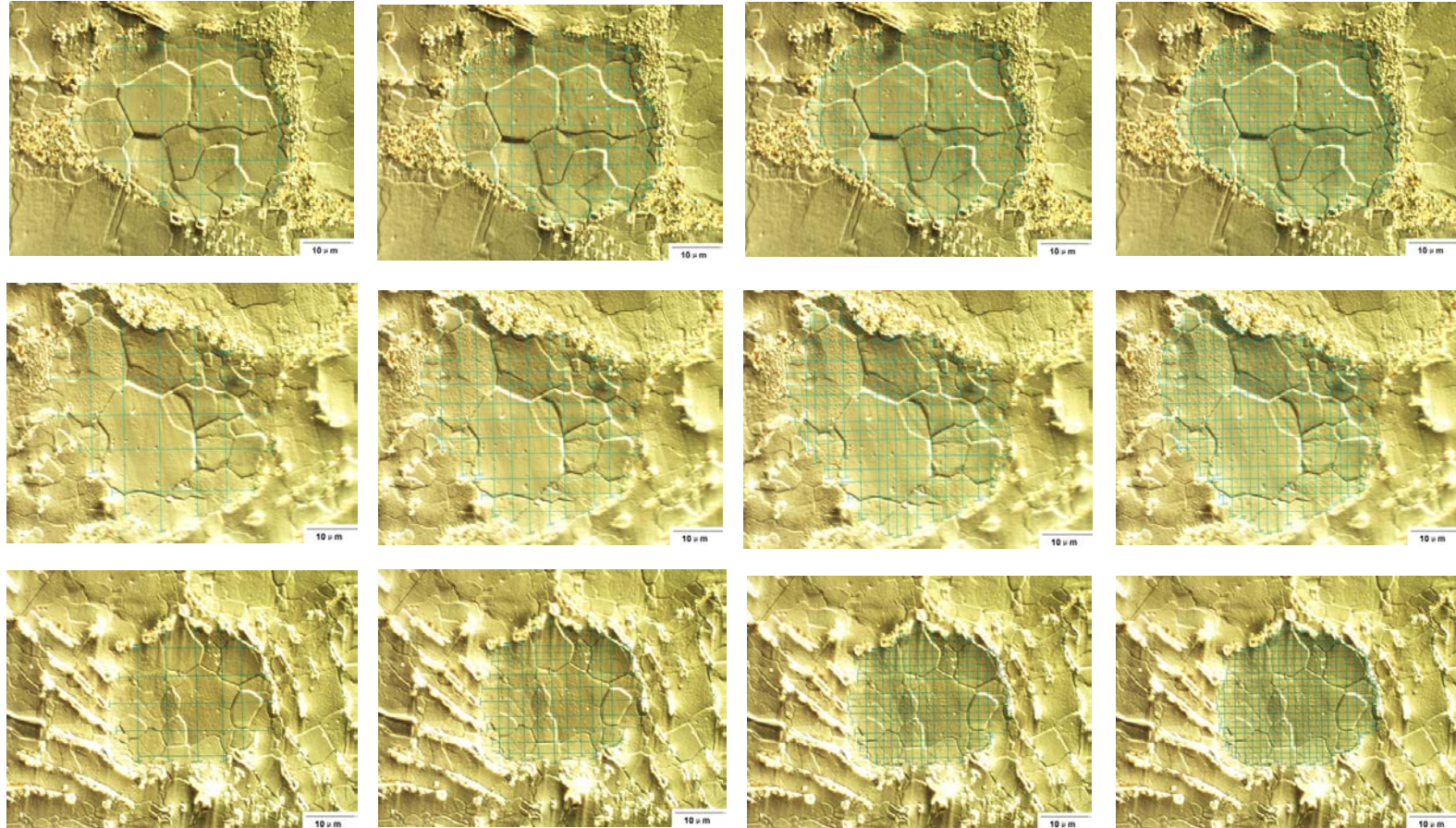
APPENDIX I

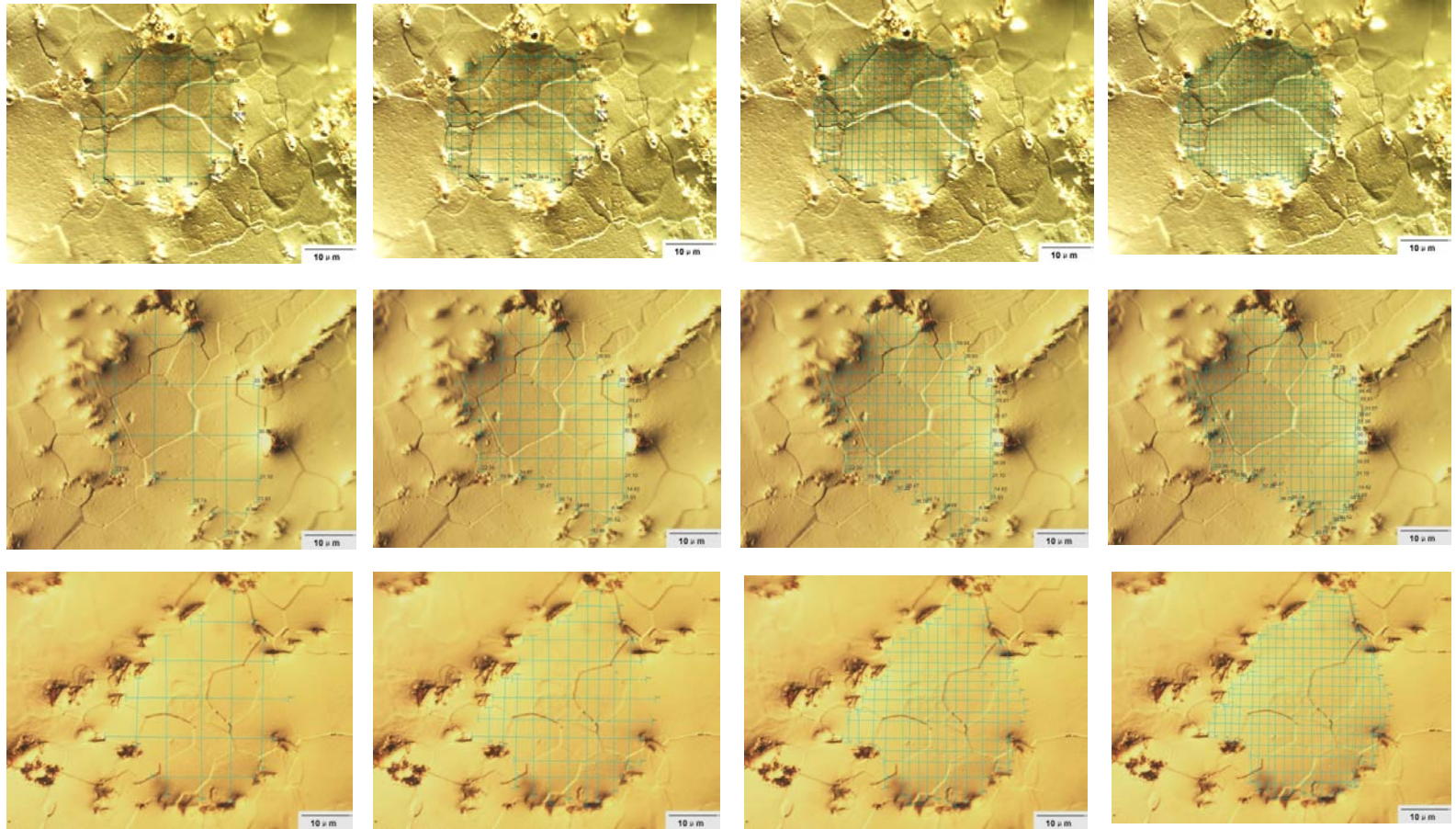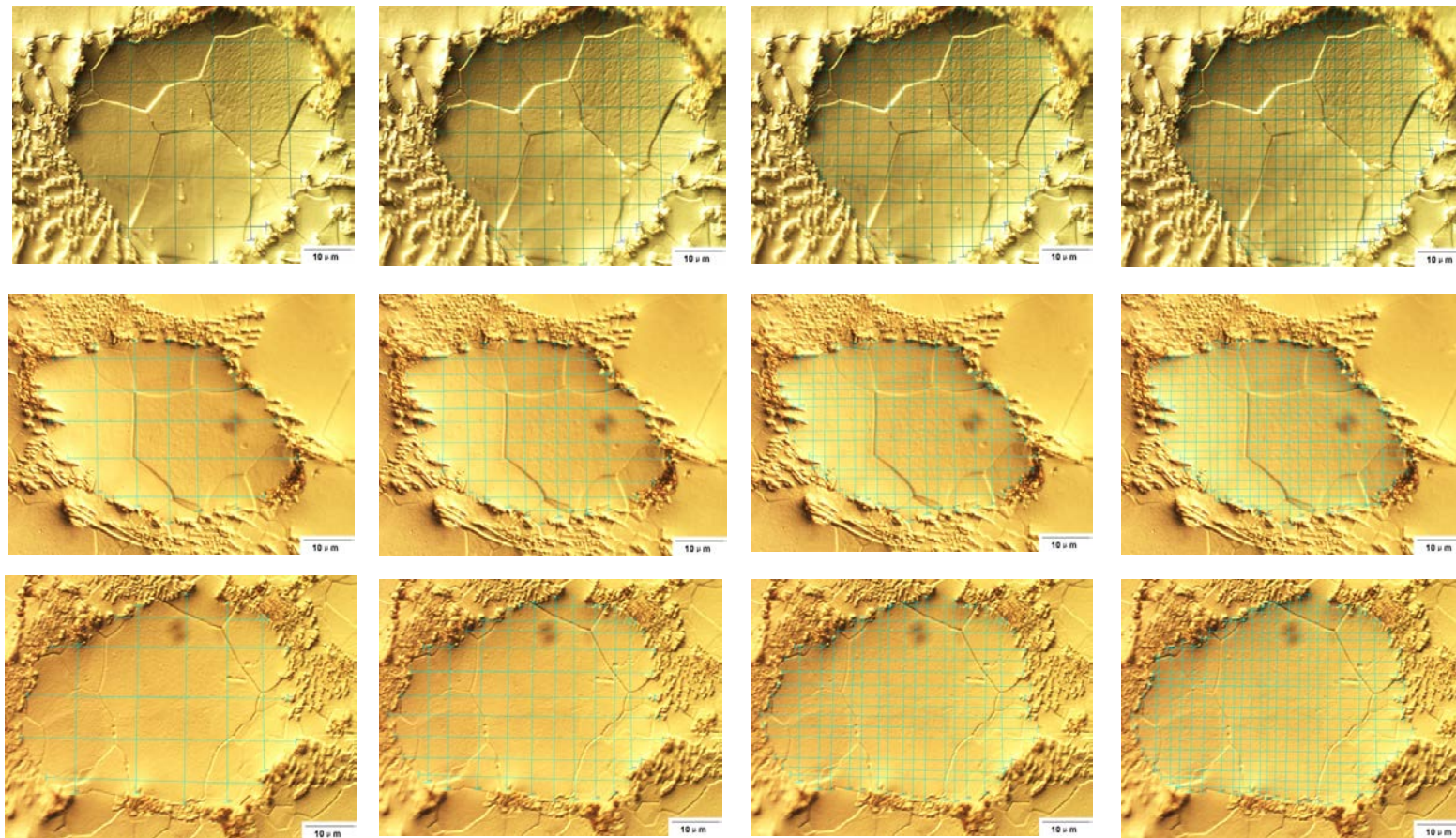## Effect of Aging Time on Sub-grain Size of SACX (Aging at 125 ºC)
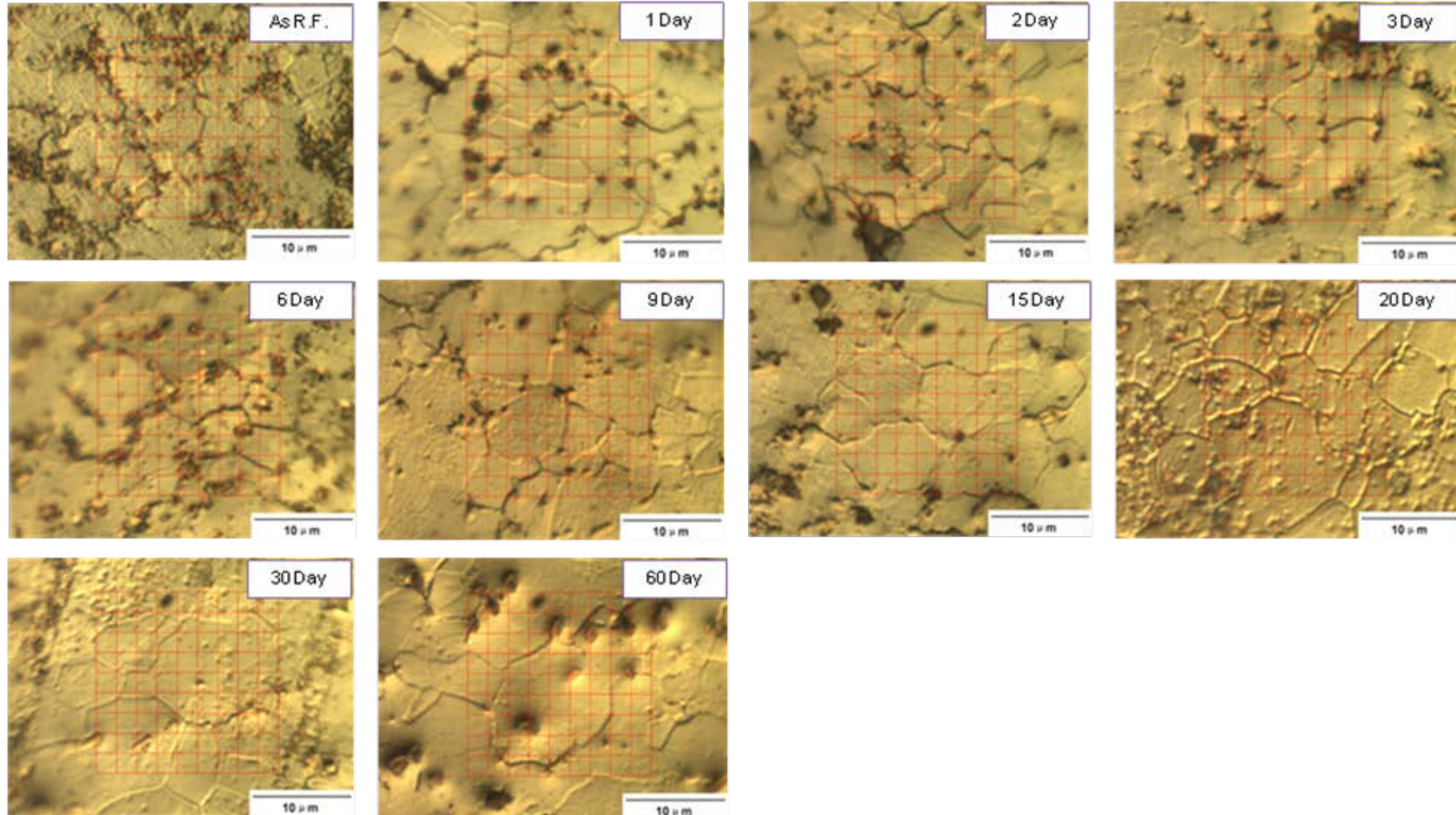
Effect of Aging Temperature on Sub-grain Size of SACX (No Aging, Aging at 25 ºC and Aging at 125 ºC)

(a) SACX without Aging (5 x 5, 10 x 10, 15 x 15, 20 x 20 Meshing)

(b) SACX with 1 Month Aging at 25 °C (5 x 5, 10 x 10, 15 x 15, 20 x 20 Meshing)

(c) SACX with 1 Month Aging at 125 ^{o}C (5 x 5, 10 x 10, 15 x 15, 20 x 20 Meshing)

APPENDIX III

Matlab Code for Stereographic Projection of β-Sn

Clear all; close all; clc;

% Enter Plane Information (h k l)

h=-4.5590;

k=0.0962;

l=1.9830;

% Enter the lattice parameter of tetragonal β-Sn structure with a = 0.58197 nm, c = 0.31749 nm

a=0.58197;

c=0.31749;

% Determine the location of the point of plane (h k l) at the distance to the origin L with angle alpha at the graph of stereographic projection of β-Sn

cosphi=sqrt((h^2+k^2)/a^2)/sqrt(l^2/c^2+(h^2+k^2)/a^2);

tanhalfphi=sqrt((1-cosphi)/(1+cosphi));

L=(1-tanhalfphi)/(1+tanhalfphi)

alpha=atan(h/k)/pi*180